photochem

MDPI

Review

Recent Advances in the Photocatalytic Reduction of Hexavalent Chromium Using Mesoporous Materials: A Review

Evangelia Barla [1], Apostolos Ioakeimidis [2], Stelios A. Choulis [2] and Ioannis T. Papadas [1,*]

[1] Department of Public & Community Health, School of Public Health, University of West Attica, 11521 Athens, Greece; ebarla@uniwa.gr
[2] Molecular Electronics and Photonics Research Unit, Department of Mechanical Engineering and Materials Science and Engineering, Cyprus University of Technology, Limassol 3603, Cyprus
* Correspondence: ipapadas@uniwa.gr

Abstract

The hazards associated with hexavalent chromium, Cr(VI), have prompted extensive research into treatment technologies for chromium-containing industrial effluents. Selection of an appropriate process depends on wastewater composition, treatment objectives, cost-effectiveness, operational feasibility, and monitoring and maintenance requirements. Mesoporous materials, with pore diameters of 2–50 nm, offer accessible surfaces and pore networks that can support adsorption and photocatalytic reactions. Following the independent discovery of ordered mesoporous materials in the early 1990s by researchers at Mobil and other research groups, their tunable physicochemical properties have supported applications across environmental catalysis. In Cr(VI) photoreduction, accessible surface area, pore connectivity, and surface functionality influence chromium-oxyanion adsorption and reactant transport, while semiconductor composition and interfacial architecture govern light absorption and charge-carrier behaviour. This review examines recent advances in mesoporous photocatalysts for Cr(VI) reduction, focusing on the relationships between pore structure, chemical composition, and reported treatment performance. Metal oxides, carbon-based composites, metal–organic and covalent organic frameworks, and heterostructured systems are discussed alongside strategies involving doping, sensitisation, and interfacial engineering. Particular attention is given to distinguishing adsorption and direct photolysis from photocatalytic reduction and to interpreting performance under different irradiation, pH, and electron-donor conditions. The reviewed literature indicates that mesostructuring can enhance photoreduction when accessible pores are combined with suitable surface chemistry and efficient charge utilisation. However, differences in experimental conditions limit direct comparison between materials. Catalyst recovery, aqueous stability, metal leaching, realistic wastewater matrices, and reactor design remain central considerations in translating laboratory performance into sustainable treatment applications.

Keywords: photocatalysis; photocatalytic reduction; mesoporous materials; heavy metal; hexavalent chromium; adsorption; wastewater treatment; catalyst; nanomaterials

Check for updates

Academic Editors: Wengjing Xiao, Massimo La Deda and Bishweshwar Pant

Received: 5 August 2026
Revised: 22 October 2026
Accepted: 28 October 2026
Published: 4 November 2026

Copyright: © 2026 by the authors. Licensee MDPI, Basel, Switzerland. This article is an open access article distributed under the terms and conditions of the Creative Commons Attribution (CC BY) license.

1. Introduction

Chromium is a widespread heavy metal contaminant in aquatic ecosystems. Chromium occurs primarily in two environmentally important oxidation states: Cr(III) and Cr(VI). Cr(VI) compounds generally exhibit greater toxicity and mobility than Cr(III) compounds and are associated with mutagenic and carcinogenic effects [1,2]. Wastewater containing Cr(VI) is discharged from industrial processes including electroplating, leather tanning,

textile dyeing, pigment production, metallurgy, and chromate manufacturing [1,2]. Applicable limits vary by jurisdiction and water-use category; limits for total chromium should be distinguished from those for Cr(VI) [1,2].

The demand for sustainable wastewater treatment processes is rising due to increasing pressure on global water resources. It has been estimated that changes in the global water cycle will result in major risks to human health, food security, economic development, and ecosystem sustainability [3]. This has intensified research into eco-friendly, cost-effective, and energy-efficient wastewater reclamation processes. Reduction of Cr(VI) to less toxic Cr(III) is one of the most widely used chromium removal methods. Since Cr(VI) is far more toxic than Cr(III) [1,2], Cr(III) can be precipitated as $Cr(OH)_3$ under controlled pH conditions and then removed from aqueous solutions [1]. Various conventional methods, such as chemical reduction, adsorption, ion exchange, membrane separation, and electrochemical methods, have been successfully used to remove Cr(VI). Nevertheless, they generally have drawbacks, including large dosages of chemicals, secondary pollutant generation, sludge production, operational complexity, and high treatment costs [1,2]. These limitations have prompted research into advanced treatment techniques capable of efficiently and sustainably removing Cr(VI).

Among emerging remediation technologies, photocatalytic reduction has attracted interest as a light-driven route for converting Cr(VI) to Cr(III), including systems designed to utilise solar irradiation. Light absorption by a semiconductor generates electron–hole pairs; photogenerated electrons participate in Cr(VI) reduction, while holes are consumed by oxidation of water or organic species [2]. Photocatalysis can operate under mild conditions and may reduce chemical demand when suitable electron donors or oxidizable co-pollutants are available. These advantages depend on catalyst stability, irradiation conditions, and the composition of the treated water, rather than being inherent to every photocatalytic system. Consequently, evaluating Cr(VI) remediation requires consideration of both the reduction reaction and the associated oxidation process, together with subsequent management of the Cr(III) product [1,2].

A schematic representation of the light absorption process and the corresponding band structure involved in photocatalytic reactions is presented in Figure 1.

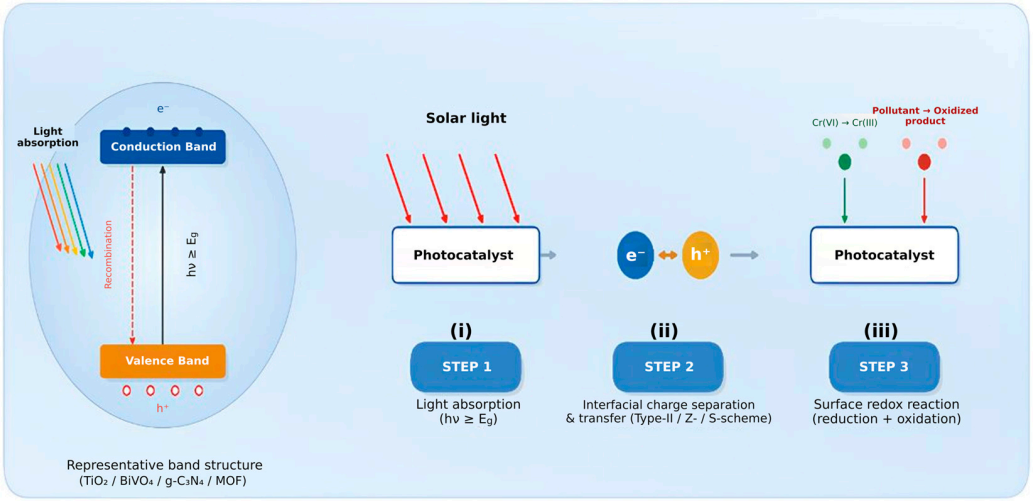


Figure 1. Schematic illustration of the general photocatalytic mechanism for Cr(VI) reduction: (**i**) light absorption and photoexcitation across the band gap, (**ii**) interfacial charge separation and transfer, and (**iii**) surface redox reactions reducing Cr(VI) to Cr(III) while oxidising an organic pollutant/hole scavenger (schematic overview; see Ref. [2]).

Despite recent improvements, challenges remain, including catalyst recovery, photocorrosion, sustainability, metal leaching, treatment of industrial wastewater, and scale-up. These issues have been addressed in recent studies through approaches such as developing magnetic composites that facilitate catalyst recovery [4], heterojunction design to improve charge separation [2], and incorporation of MXenes into photocatalytic composites to improve interfacial charge transfer [5,6].

Metal–organic frameworks (MOFs) represent a particularly versatile class of porous materials with tunable photocatalytic properties. Frameworks containing mesopores can offer additional transport advantages, although MOFs are not intrinsically mesoporous. MOFs are crystalline porous materials constructed from metal nodes and organic linkers, offering controllable pore size, tunable pore surface chemistry, low density, and exceptionally high surface area. These features enable MOFs to be widely applied in adsorption, photocatalysis, and heterogeneous catalysis. In the context of Cr(VI) reduction, MOFs provide opportunities for functionalization (e.g., amino groups) that extend light absorption into the visible range and enhance selective binding of chromium oxyanions. Their structural diversity and modular design make them promising candidates for scalable photocatalytic systems [1,7,8]. Mesoporosity should therefore be established from measured pore-size distributions rather than inferred solely from a high BET surface area [9].

Heterostructured photocatalysts represent a critical design strategy for Cr(VI) reduction because they can promote improved charge separation and broadened light absorption through engineered band alignment. Comparative studies show that type-II heterojunctions, such as mesocrystalline anatase coupled with $SrTiO_3$ nanodots [10], achieve higher efficiencies under simulated solar radiation by combining enhanced adsorption capacity with effective electron–hole separation. Z-scheme and S-scheme architectures are also investigated to retain strongly reducing electrons and strongly oxidising holes [2]. In Z-scheme systems, selective recombination of photogenerated electrons in one semiconductor with holes in the other retains charge carriers with strong reduction and oxidation abilities. The S-scheme model describes this selective interfacial recombination by explicitly considering charge redistribution upon contact, the resulting built-in electric field, and band bending [11]. For example, a three-dimensional Bi_2S_3–$BiVO_4$ graphene aerogel was investigated for simultaneous Cr(VI) reduction and bisphenol A degradation under visible light [12]. Such comparisons require attention to the reported reaction conditions.

Mechanistic validation is critical in these systems. Photoluminescence quenching, transient photocurrent response, and electrochemical impedance spectroscopy provide complementary evidence of altered carrier dynamics in heterostructures compared to single-phase catalysts. Radical-trapping experiments can help elucidate the roles of reactive species, while XPS analysis can provide evidence for the presence of Cr(III) on the catalyst surface, supporting the mechanistic interpretation of Cr(VI) reduction. Stability assessments also reveal that heterostructures generally retain >80% activity after multiple cycles, whereas single-phase catalysts often suffer from photocorrosion or agglomeration. These measurements should be interpreted together with chromium speciation and mass-balance data; carrier measurements alone do not establish complete conversion or a unique charge transfer pathway [2].

Overall, heterostructure design provides a pathway to enhance Cr(VI) photoreduction. Type-II systems emphasise efficient charge separation, Z-schemes preserve strong redox potentials, and S-schemes combine both advantages. Future studies should systematically benchmark band alignment, kinetic constants, and long-term stability to ensure reproducibility and mechanistic validation. Related host–guest engineering has been investigated for H_2 evolution [13], and interface and vacancy engineering for H_2O_2 photoproduction [14,15].

These applications provide background design principles rather than direct evidence of Cr(VI) reduction.

This review focuses on how mesoporous structure affects photocatalytic Cr(VI) reduction. The materials are discussed in terms of pore accessibility, surface chemistry, and charge-carrier behaviour, with attention to the experimental evidence supporting the proposed structure–performance relationships. Recovery, stability, and scale-up are also examined because high laboratory conversion does not by itself establish practical suitability. Reported efficiencies are considered together with irradiation conditions, solution chemistry, and control experiments. The aim is to identify where mesoporous design contributes to treatment performance, where its contribution remains uncertain, and which experimental and reactor considerations deserve further investigation in wastewater applications.

The discussion begins with chromium speciation and the fundamentals of photocatalytic reduction, followed by the roles of pore architecture, surface chemistry, and material composition. Representative mesoporous photocatalysts are then examined in relation to their mechanisms and reported performance. Finally, catalyst stability, recovery, reactor design, and wastewater applications are considered together to connect material properties with practical treatment requirements.

2. Review Methodology

A literature review was conducted to identify primary research articles and review articles related to photocatalytic reduction of hexavalent chromium, Cr(VI), using mesoporous materials. The Scopus database was selected for this literature search because of its broad coverage of scientific literature in materials science, environmental chemistry, and photocatalysis. The search was conducted in May 2026 using the following Boolean query: (Photocatalysis OR "photocatalytic reduction") AND ("hexavalent chromium" OR "Cr(VI)" OR "Cr^{6+}") AND (mesoporous OR porous OR heterojunction OR "metal-organic framework" OR MOF OR "g-C_3N_4" OR "graphitic carbon nitride" OR MXene OR COF OR "covalent organic framework"). Additional references were incorporated during manuscript revision in October 2026 to support the general discussion and provide mechanistic context; these were not included in the dataset of 93 studies.

In this systematic review, the literature was retrieved from the Scopus database using a Boolean search string applied in May 2026, covering the period 2013–May 2026. The initial search identified 249 records, which were screened in successive stages. After removal of duplicates, 151 records remained. Title and abstract screening reduced this number to 107. Of these, 13 records could not be retrieved in full text despite repeated attempts through institutional access and interlibrary requests, and were therefore excluded. This left 94 studies available for full-text eligibility assessment. One article was subsequently excluded because it lacked mechanistic or mesoporosity characterisation, resulting in a final dataset of 93 studies.

The original selection considered both peer-reviewed primary research and review articles; primary research articles provide the experimental comparisons in this review. Assessment of mesoporosity requires pore-size characterisation for the specific material; a high BET surface area alone is insufficient. Relevant descriptors include BET surface area, pore-size distribution, Cr(VI) treatment performance, light source, pH and control experiments. Missing parameters are identified as "not reported" rather than inferred.

Review articles were used to frame the field and identify research gaps but were not tabulated as primary experimental studies. Related porous composites discussed for mechanistic context should not be interpreted as confirmed mesoporous materials unless the original publication provides suitable pore characterisation. The bibliography also

includes reviews and contextual sources and therefore differs in size from the screened study dataset.

The following information was extracted from the primary experimental articles: authors, year, and journal; the composition and structure of the photocatalysts; the specific surface area (BET, m^2/g) and the pore size (nm) described; chromium removal percentage (%) or the rate constant (min^{-1}); experimental conditions such as the initial Cr(VI) concentration, amount of catalyst used, pH, light source, irradiation period, and the presence or absence of a hole scavenger; reusability and stability information (cycles and activity percentage retained); and the proposed mechanisms (heterojunction formation and charge transfer processes).

The studies included in the summary tables (Section 5) were selected based on the availability of key parameters, including BET surface area, pore size distribution, Cr(VI) removal efficiency or rate constant, light source, and pH conditions. Where relevant, related porous and composite photocatalysts were also included for descriptive comparison; a high BET surface area alone was not treated as proof of mesoporosity. Studies lacking sufficient pore characterisation were interpreted separately in the qualitative discussion of photocatalytic performance and mechanisms. Any information not reported in the original articles is indicated as "not reported" in the tables.

Quantitative entries are linked to their source publications and must be interpreted with the corresponding catalyst loading, irradiation conditions, reaction time, solution composition, and analytical endpoint. Unavailable parameters are marked as "not reported." The comparison of commercial TiO_2 samples distinguishes unnormalized performance from surface-area-normalised rates: ST-01 showed the highest unnormalized rate in the study by Islam et al. [16], whereas P25 showed the highest surface-area-normalised rate. Cr(VI) disappearance, total chromium removal and confirmed conversion to Cr(III) are distinct endpoints; the cited reference alone does not establish that they are interchangeable.

Several methodological limitations of this review should be acknowledged. First, the search used a single database (Scopus), so some relevant articles indexed in other databases may not have been included in the analysis. Second, excluding studies published in languages other than English may introduce language bias; nonetheless, there were only two such articles found ($n = 2$). Finally, 13 articles could not be retrieved in full text despite repeated attempts through institutional access and interlibrary requests, resulting in availability bias. Furthermore, considerable variations in experimental conditions such as the light source, Cr(VI) concentration, pH, and the catalyst loading make it impossible to perform a meta-analysis of the removal efficiency.

3. Fundamentals of Photocatalytic Cr(VI) Reduction

3.1. Chromium Speciation and pH Dependence

The speciation of Cr(VI) in aqueous solutions depends on both pH and total chromium concentration, both of which influence photocatalytic efficiency. At low pH values (pH 1–6), $HCrO_4^-$ is important, while $Cr_2O_7^{2-}$ becomes more significant as concentration increases. Acidic conditions often favour reduction and adsorption onto protonated catalyst surfaces; the standard potential of the $Cr_2O_7^{2-}/Cr^{3+}$ couple is approximately +1.33 V versus NHE under standard acidic conditions [1,2]. In contrast, CrO_4^{2-} is more abundant at high pH (pH > 7), while the reduction potential and adsorption behaviour depend on the half-reaction, solution composition, and catalyst point of zero charge [1,2]. For these reasons, most Cr(VI) photocatalytic reduction experiments are carried out at low pH values (pH 2–3), but wastewater may have near-neutral pH, necessitating further development of catalysts capable of performing well under such conditions [1,2].

3.2. Definition of Mesoporosity

Porous materials can be classified into three broad categories (i.e., microporous, mesoporous, and macroporous) based on the range of pore sizes defined by IUPAC: microporous (below approximately 2 nm), mesoporous (approximately 2–50 nm), and macroporous (above approximately 50 nm). Mesoporous materials have attracted considerable attention for photocatalytic applications because they can combine high specific surface areas with accessible active sites and pore dimensions intermediate between those of microporous and macroporous materials [9].

3.3. Role of Mesoporosity in Photocatalysis

Mesoporous architectures can offer advantages for photocatalytic Cr(VI) reduction by increasing accessible surface area, facilitating transport through connected pores, and providing surfaces for functionalization or heterojunction construction. The extent of these benefits depends on pore accessibility, surface chemistry, and the optical and electronic properties of the constituent materials; mesoporosity alone does not ensure improved photocatalytic activity.

(i) High specific surface area: Mesoporous catalysts can possess high BET specific surface areas (ranging from 100 to 1500 m^2/g), which can favour Cr(VI) adsorption on their surface and provide more reactive sites for photoreduction reactions [1,9]. For instance, NH_2-MIL-125(Ti) has been reported to have an exceptionally large surface area of 1343.9 m^2/g and enhanced visible-light Cr(VI) photoreduction [7]. Likewise, mesoporous CuO/ZrO_2 MCM-41 nanocomposites exhibited a surface area of ~700 m^2/g and achieved nearly complete Cr(VI) photoreduction under visible light irradiation, as reported by Nanda et al. [17].

The reported surface areas help explain the interest in these materials for adsorption-assisted photoreduction. More accessible surface can improve contact between chromium oxyanions and the photoactive phase, although adsorption capacity is not a direct measure of light-driven conversion. Pore accessibility and surface chemistry remain important when interpreting the results obtained under different irradiation conditions [1,2,9].

(ii) Interconnected pore network: The porous nature of titanium dioxide and zirconium dioxide nanocomposites can facilitate rapid diffusion of Cr(VI) species to the catalytic sites while facilitating release of the Cr(III) product from these catalytic sites, although deposited products may block pores and affect catalytic activity during repeated catalytic reactions. In their investigation of complete Cr(VI) removal using titanium dioxide and zirconium dioxide nanocomposites, Yan et al. [18] examined composites with mesopores around 4.5 nm and assessed their reuse over four cycles. A particular pore diameter should not be treated as a universal requirement for complete removal.

(iii) Confinement within mesopores helps stabilise small nanoparticles and limit their agglomeration while potentially influencing charge separation through interfacial contact and carrier-transport pathways [1,17]. Confinement can be particularly beneficial for semiconductor quantum dots and metal clusters. In a related approach, the use of ZnSe nanoparticles immobilised on mesoporous TiO_2 resulted in a Cr(VI) photoreduction rate of 177 μmol/min with visible light [19].

(iv) The tunable pore structure of mesoporous materials allows for the functionalisation of mesopore surfaces with specific chemical groups (e.g., $–NH_2$, –COOH, –SH) that modify interactions with Cr(VI) oxyanions, which can enhance the rate and selectivity of Cr(VI) adsorption and reduction [1,7]. For example, amino-functionalised MOFs such as NH_2-MIL-125(Ti) and UiO-66(NH_2) can have extended visible-light absorp-

tion through framework-dependent ligand–metal charge transfer processes, thereby enabling photocatalytic activity under visible light [1,8].

The structure–performance relationship is central to understanding Cr(VI) photoreduction. Larger accessible surface areas can increase adsorption capacity and provide more active sites, while pore size and connectivity determine ion diffusion and product release. Functional groups such as $–NH_2$ or –COOH can modify chromium-oxyanion binding; their effects depend on protonation state and surface chemistry. Changes in visible-light absorption additionally depend on the electronic structure of the framework. Together, these parameters dictate how efficiently mesoporous catalysts combine adsorption and photocatalysis, underscoring the importance of tailoring pore architecture and surface chemistry for optimal Cr(VI) reduction. These effects require material-specific characterisation and suitable controls [1,2,9].

3.4. Photocatalytic Mechanism and Kinetics

The photocatalytic reduction of Cr(VI) is frequently described by apparent pseudo-first-order kinetics within a defined concentration range and under specified irradiation conditions [2,16]. However, mechanistic validation requires more than simplified equations. A comprehensive mechanistic framework must integrate balanced half-reactions, spectroscopic and electrochemical evidence, and adsorption/photolysis controls.

3.4.1. Mechanistic Pathways and Experimental Evidence

Upon photoexcitation, semiconductor catalysts generate electron–hole pairs.

$$\text{Semiconductor} + h\nu \rightarrow e^-_{CB} + h^+_{VB} \quad (1)$$

The photogenerated electrons reduce Cr(VI) species, while holes are consumed through the oxidation of water or sacrificial electron donors. Experimental techniques provide complementary information about these processes: PL quenching, transient photocurrent response, and EIS probe carrier behaviour, while radical trapping, XPS, chromium speciation, and mass balances support mechanistic assignments. None of these carrier measurements alone proves complete reduction [2].

3.4.2. Balanced Half-Reactions (pH-Dependent)

The shorthand expression "Cr(VI) + $3e^-$ → Cr(III)" oversimplifies the chemistry. Cr(VI) reduction depends strongly on pH and speciation:

At low pH ($HCrO_4^-$ dominant):

$$HCrO_4^- + 7H^+ + 3e^- \rightarrow Cr^{3+} + 4H_2O \quad (2)$$

For dichromate-containing acidic solutions (concentration-dependent speciation):

$$Cr_2O_7^{2-} + 14H^+ + 6e^- \rightarrow 2Cr^{3+} + 7H_2O \quad (3)$$

At neutral/alkaline pH (CrO_4^{2-} dominant):

$$CrO_4^{2-} + 4H_2O + 3e^- \rightarrow Cr(OH)_3(s) + 5OH^- \quad (4)$$

These balanced half-reactions account for the different chromium species and proton/hydroxide balances under acidic and neutral/alkaline conditions.

3.4.3. Adsorption, Photolysis, and Photocatalysis Controls

Mechanistic reliability requires distinguishing adsorption and photolysis from true photocatalysis.

- Dark controls: Skliri et al. [20] reported that Cr(VI) reduction did not proceed in the dark under the tested conditions.
- Photolysis controls: Catalyst-free irradiation controls are needed to determine whether direct photolysis contributes to the observed Cr(VI) removal [2].
- Photocatalysis: The optimised $MnFe_2O_4$–$ZnFe_2O_4$ composite achieved >99% Cr(VI) reduction after 3 h of irradiation at $\lambda > 360$ nm in the presence of phenol [20].

Tables should therefore not only mark "dark adsorption + photolysis" but also report the quantitative extent of removal in each control, where reported, ensuring mechanistic clarity.

3.5. Simultaneous Cr(VI) Reduction and Organic Oxidation

An integrated approach to wastewater treatment combines Cr(VI) reduction and organic pollutants oxidation within a single photocatalytic system. In this dual-function system, photogenerated electrons reduce Cr(VI) to Cr(III), while photogenerated holes can oxidise organic contaminants, such as dyes, phenols, and antibiotics. This coupling can facilitate the utilisation of photogenerated charge carriers and promote the simultaneous Cr(VI) reduction and organic pollutant degradation from contaminated water matrices [2,21]. Zhang et al. [2] reviewed the potential of this approach for coupled pollutant removal. The general principles of the simultaneous removal process are depicted in Figure 2.

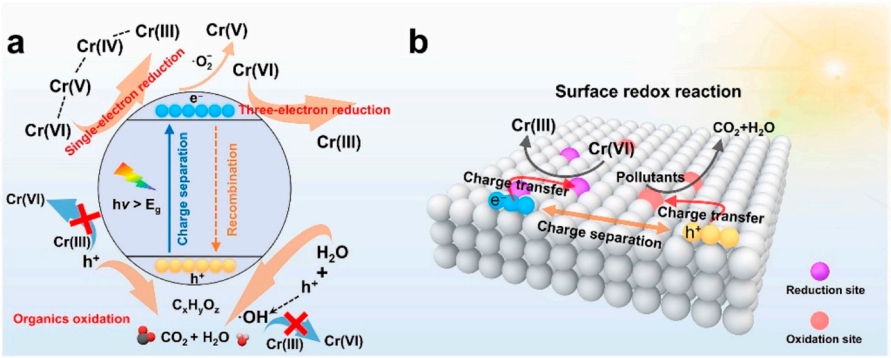


Figure 2. Schematic illustration of the basic principles of simultaneous removal of Cr(VI) and organic pollutants. (**a**) Band structure; (**b**) surface reactions. Red crosses indicate suppression of Cr(III) reoxidation to Cr(VI) by holes and hydroxyl radicals. Cyan and yellow spheres represent electrons (e−) and holes (h+), respectively; purple and pink spheres in (**b**) mark reduction and oxidation sites. The blue upward and orange dashed downward arrows in (**a**) denote charge separation and recombination, respectively; the multicoloured arrow represents incident light. Reproduced from open-access Ref. [2].

3.6. Role of Hole Scavengers and Adsorption

Hole scavenging can improve photocatalytic Cr(VI) reduction efficiency. In this regard, organic acids such as formic, citric, and oxalic acids, as well as alcohols such as ethanol and methanol, have been extensively used as sacrificial reagents to consume photogenerated holes and extend electron lifetimes, thereby enhancing Cr(VI) reduction efficiency [1,2]. For example, Islam et al. [16] observed an enhanced Cr(VI) reduction rate using nanosized TiO_2 in the presence of formic acid, which acts as an effective hole scavenger. Likewise, Wang et al. [7] compared ethanol, citric acid, and EDTA for NH_2-MIL-125(Ti), showing that donor selection influenced performance and that ethanol gave the strongest enhancement in the comparison displayed. Beyond conventional organic scavengers, Huang et al. [22] recently demonstrated that iodide and sulphite act synergistically to enhance Far-UVC-driven Cr(VI) reduction even under alkaline conditions, expanding the operational pH

range for photochemical reduction. This homogeneous process should be distinguished from semiconductor photocatalysis.

Adsorption can also influence the observed Cr(VI) removal, particularly in mesoporous materials with high accessible surface areas. Depending on solution pH and surface chemistry, Cr(VI) oxyanions can adsorb onto catalyst surfaces under dark conditions. The process can involve (i) adsorption of Cr(VI) species onto the catalyst surface and (ii) their subsequent photocatalytic reduction to Cr(III) under illumination. Dark controls and irradiation experiments without the catalyst are therefore needed to distinguish adsorption and catalyst-free photochemical processes from photocatalytic reduction. Whether dark adsorption and catalyst-free irradiation controls were reported for each study. Where available, these controls and their outcomes are noted; otherwise, the information is marked as "not reported". This distinction helps assess the contribution of photocatalytic reduction to the observed Cr(VI) removal.

4. Mesoporous Photocatalyst Materials for Cr(VI) Reduction

4.1. Titanium Dioxide and Metal Oxide-Based Photocatalysts

Titanium dioxide (TiO_2) is widely investigated for Cr(VI) reduction because of its relatively low cost, chemical stability, and photocatalytic activity under UV irradiation. Its practical utilisation is constrained by predominantly UV-driven excitation and rapid electron–hole recombination. Modification strategies address different aspects of these limitations: mesostructuring can increase accessible surface area and active-site exposure; doping and sensitisation can modify the spectral response; and composite formation introduces interfaces that influence charge separation and transport. These strategies can be complementary, although their effectiveness depends on the resulting textural, optical, and electronic properties rather than on structural complexity alone. Accordingly, the performance of modified TiO_2 should be interpreted in relation to the specific function of each introduced component [2,16].

Mesostructuring introduces pores that can increase the surface accessible for adsorption and interfacial photoreduction. Loryuenyong et al. [23], for example, used activated carbon as a template to prepare mesoporous anatase TiO_2 nanoparticles with higher Cr(VI) removal than commercial P25. The resulting pore architecture provides a basis for examining how surface accessibility influences dichromate adsorption and reduction. Such comparisons support the potential of mesostructuring, while also requiring attention to differences in crystallinity, surface chemistry, and optical response. Enhanced removal should therefore be attributed to the combined properties of the prepared material rather than to pore formation in isolation.

Doping semiconductors with suitable non-metal species, such as nitrogen, carbon, and sulphur, or with transition metals can introduce electronic states within the band gap or modify the band-edge positions, potentially extending the optical response into the visible region. These effects depend on the host material, dopant, and doping level; dopant-related states can also act as charge-recombination centres. For TiO_2-based materials, Jin et al. [24] investigated Si/N-modified TiO_2 nanocrystals for visible-light-driven reduction of Cr(VI) at concentrations in the g L^{-1} range, while Zhai et al. [25] studied N–TiO_{2-x}@C nanocomposites for treating highly concentrated chromium-containing wastewater. These examples indicate that photocatalytic performance depends on the combined effects of light absorption, surface chemistry, defects, and charge transport [24,25].

Furthermore, black Zr-TiO_2 nanotube arrays have shown high Cr(VI) reduction rates, as reported by Wang et al. [26] (2021). Surface sensitisation represents an alternative approach in which light-absorbing species, such as dye molecules or quantum dots, are coupled to the photocatalyst surface to extend light absorption and facilitate charge transfer.

Yang et al. [27] prepared mesoporous TiO_2 with chlorophyll incorporated in situ, exhibiting absorption bands around 407 and 668 nm. Under visible-light irradiation and without an added hole scavenger, the composite achieved 86.1% Cr(VI) photoreduction, approximately 20 times that obtained with TiO_2 bearing physically adsorbed chlorophyll and 29 times that obtained with TiO_2 without chlorophyll. These results support the beneficial role of in situ chlorophyll incorporation and confinement in this system [27]. Other sensitisers include molecular dyes, conducting polymers, and quantum dots, although their stability under irradiation requires consideration.

Combining TiO_2 with carbon materials or noble metals can improve photocatalytic performance. Activated carbon, rGO, and graphene may enhance adsorption and facilitate electron transfer, potentially reducing charge-carrier recombination [28–30].

Beyond these systems, Shan et al. [31] investigated TiO_2 anchored on MoS_2 nanosheets as a photocathode for enhanced Cr(VI) reduction in a microbial fuel cell. This photoelectrochemical application should be distinguished from photocatalysis in catalyst suspensions. Wang et al. [32] also investigated a TiO_2/rGO/CuO composite for visible-light-driven Cr(VI) reduction.

In the activated-carbon-supported photocatalysts studied by Tu et al. [28], the support contributes to adsorption while the photoactive phase enables light-driven reduction. Contact between these components is therefore relevant to the overall reaction. Similar considerations apply to more complex architectures: additional components can be beneficial when they improve access to reactive sites, facilitate charge transfer, or help retain activity during reuse. Increasing the number of phases alone offers no assurance of better performance.

To assess whether these architectural changes are responsible for improved performance, the contributions of charge separation, active-site accessibility, and mass transfer should be considered separately. Comparisons with individual components and appropriate control materials are needed to distinguish these effects from changes in experimental conditions [2].

Cao et al. [10] prepared heterostructures comprising mesocrystalline anatase TiO_2 submicrospheres decorated with $SrTiO_3$ nanodots, which exhibited enhanced photocatalytic Cr(VI) reduction under simulated solar irradiation. The improved performance was associated with enhanced Cr(VI) adsorption and more efficient separation of photogenerated charge carriers through a type-II heterojunction with close interfacial contact between the two phases. This example illustrates how combining TiO_2 with another semiconductor can improve photocatalytic performance through complementary surface and electronic properties [10].

The structural flexibility of MOFs and COFs provides a complementary approach to the oxide-based designs discussed above. Their pore structures and surface functional groups can influence adsorption, while the choice and modification of organic linkers can alter electronic structure and visible-light absorption. These features offer opportunities to tune active-site accessibility and electronic energy levels within the framework. Amino-functionalised MOFs [7,8] and halogen-functionalised COFs [33] illustrate how framework modification can influence light absorption, charge-carrier behaviour, and photocatalytic Cr(VI) reduction.

However, practical application requires evaluation of framework stability in aqueous media at the operating pH, resistance to photodegradation during prolonged irradiation, and retention of activity during reuse. Stability depends on the specific framework and reaction conditions and should therefore be assessed for each material. Framework stabilisation, integration with suitable supports, and scalable, cost-effective synthesis are potential strategies for advancing these materials towards wastewater treatment applications.

These examples connect the individual modification strategies discussed in this section. Mesoporosity primarily affects surface accessibility and mass transport, whereas doping, sensitisation, and heterostructure formation modify light absorption or charge-carrier behaviour. Their combined effects can improve Cr(VI) reduction, but performance should be evaluated under the relevant reaction conditions, using comparative controls to identify the contribution of each modification [2]. Conductivity, pore accessibility, and structural durability require separate characterisation. Mesoporosity should not be inferred from high surface area alone [9].

4.2. Metal–Organic Frameworks (MOFs) and Covalent Organic Frameworks (COFs)

MOFs and COFs allow the tuning of in-pore chemistry and electronic structure through the selection of nodes, linkers, and incorporated components. Their photocatalytic behaviour can therefore be examined in relation to both Cr(VI) adsorption and photoinduced charge transfer. Figures 3–5 show representative reaction profiles and characterisation results, including the effects of electron donors and solution pH on the reported Cr(VI) conversion.

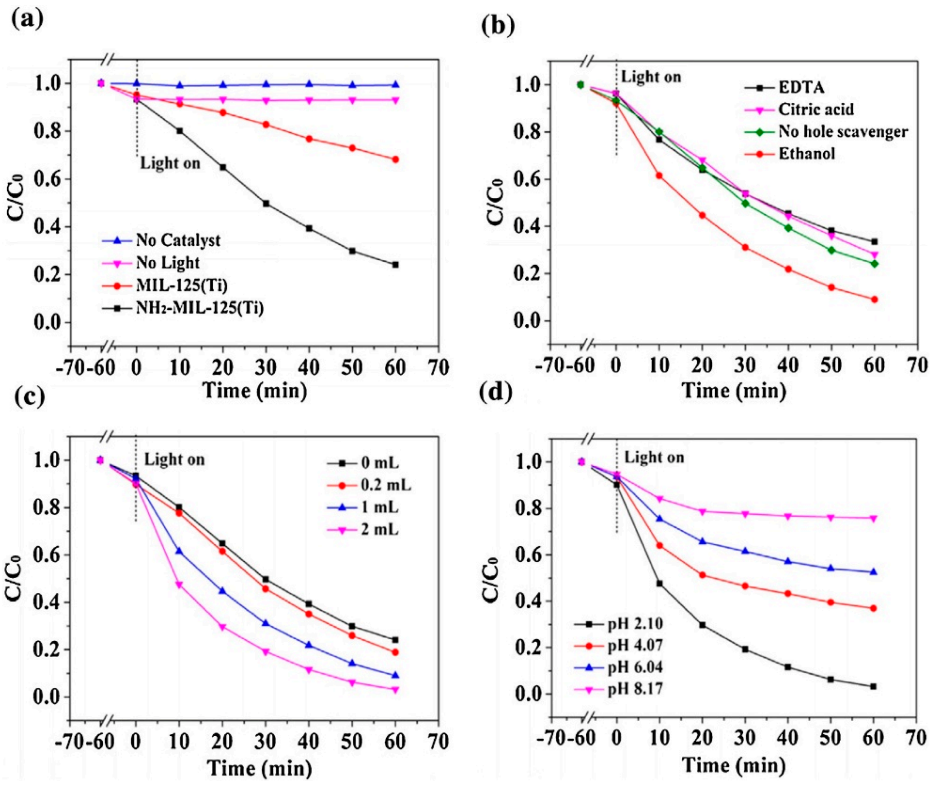


Figure 3. (**a**) Cr(VI) reaction profiles; (**b**) effects of hole scavengers; (**c**) effect of ethanol addition; and (**d**) effect of solution pH for NH_2-MIL-125(Ti). Reproduced from the review by Wang et al. [1]; the underlying experimental study is Wang et al. [7].

NH_2-MIL-125(Ti) (BET surface area: 1343.9 m^2/g, pore size: 2.05 nm) maintained a Cr(VI) reduction efficiency of approximately 91% over 3 consecutive cycles under visible light irradiation at pH 2.1 [7]. UiO-66(NH_2) (BET surface area: 1123 m^2/g, pore size: 2.1 nm) similarly maintained a Cr(VI) reduction efficiency of approximately 90% after 3 reuse cycles without significant photocorrosion [8]. A TiO_2/MOF-801(Zr) composite prepared by wet impregnation at room temperature has likewise been reported as a highly efficient photocatalyst for Cr(VI) reduction, illustrating the potential of combining MOF with TiO_2 nanoparticles [34]. ZnO@ZIF-8 heterostructures have demonstrated enhanced

selective photocatalytic reduction of Cr(VI) in the presence of methylene blue, attributed to the adsorption and size-selective permeation properties of the ZIF-8 shell [35]. CdS/MIL-125(Ti) heterostructures exhibited higher photocatalytic activity for Cr(VI) reduction under visible-light irradiation than pristine MIL-125(Ti) [1]. Pd@UiO-66(NH_2) and RGO/UiO-66(NH_2) exhibited complete Cr(VI) removal with superior kinetics compared with the corresponding unmodified MOFs [1].

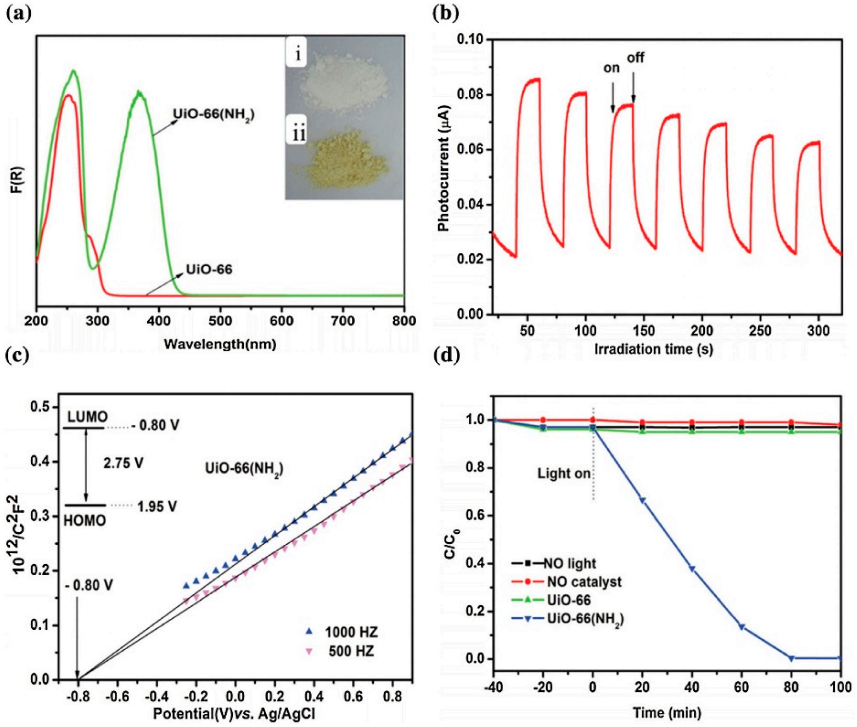


Figure 4. (**a**) UV–visible diffuse-reflectance spectra, with inset photographs showing (**i**) UiO-66 and (**ii**) UiO-66(NH_2); (**b**) transient photocurrent response; (**c**) Mott–Schottky analysis; and (**d**) Cr(VI) reaction profiles for UiO-66(NH_2). Reaction conditions: 20 mg catalyst, 40 mL of 10 mg/L Cr(VI), 100 µL methanol, 30 °C, and pH 2. Reproduced from Ref. [1]; the original study is Shen et al. [8].

Recently reported systems include NH_2-MIL-101(Fe)-$ZnIn_2S_4$ S-scheme heterojunctions (Tu et al. [36]), defect-engineered MOFs (Ma et al. [37]), and MIL-101(Fe)-g-C_3N_4 Z-scheme systems (Zhao et al. [21]). These examples highlight the versatility of MOF composites in achieving enhanced charge separation and photocatalytic efficiency. Wu et al. [38] investigated amino-functionalized MIL-68(Ga), while Liang et al. [39] examined ligand-substitution effects in MIL-68(In). Another framework modification was reported by Zhao et al. [40], who introduced WO_4^{2-} into bismuth terephthalate (BiBDC) to enhance photocatalytic Cr(VI) reduction under UV irradiation. Pore-size measurements should be considered separately for each framework and composite.

The photocatalytic performance of ZnO@ZIF-8 and ZnO was investigated via the treatment of single-solute aqueous solutions and mixed methylene-blue/Cr(VI) solutions, as illustrated in Figure 5 [35].

The stability of MOFs in aqueous environments depends on framework chemistry and reaction conditions, including solution pH. NH_2-MIL-125(Ti) and UiO-66(NH_2) have demonstrated recyclability under the conditions examined in the respective Cr(VI) photoreduction studies [7,8].

Covalent organic frameworks (COFs) provide organic networks whose linkage chemistry and degree of conjugation influence aqueous stability and photoactivity. Wang et al. [41] prepared fully conjugated, planar COFs for water purification, while Chen et al. [42] incorporated redox-active metal centres for Cr(VI) photoreduction. Donor–acceptor COFs investigated by Yue et al. [43] offered tunable visible-light performance, and Cao et al. [33] examined halogen-functionalized structures. These modifications alter the chemical environment of the photoactive framework and offer several ways to control its response to light. Their effectiveness also depends on whether the reaction solution can reach the active sites and whether the network remains stable during irradiation and repeated use.

The structural versatility of MOFs and the range of available modification methods make them promising photocatalysts. Combining MOFs with semiconductor materials or functionalizing zirconium-based MOFs with noble-metal nanoparticles illustrates how composite design can improve photocatalytic activity and enable coupled pollutant treatment [21,44]. Such approaches provide several routes for tailoring adsorption, light absorption, and interfacial charge transfer.

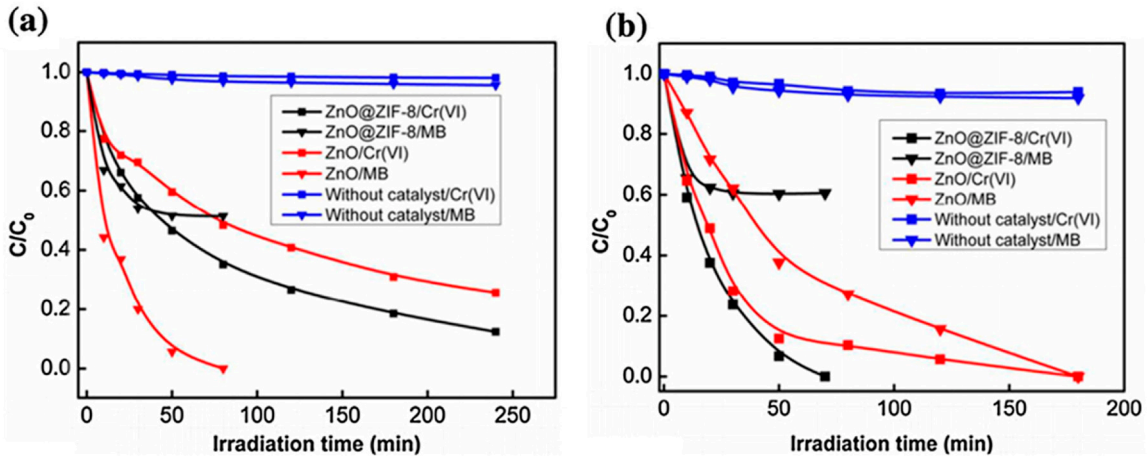


Figure 5. Photocatalytic removal profiles for Cr(VI) and methylene blue over ZnO@ZIF-8 heterostructures and ZnO spheres in (**a**) single-solute and (**b**) mixed-solute aqueous systems under UV irradiation. Reproduced from Wang et al. [35].

4.3. Heterostructured and Composite Photocatalysts

Heterostructured photocatalysts combine components with complementary optical and electronic properties to improve the utilisation of photogenerated charge carriers. Coupling wide-bandgap oxides with narrower-bandgap semiconductors can broaden the spectral response, while suitable interfacial arrangements can facilitate charge separation and transfer. These functions connect composite design with the adsorption and transport considerations discussed for mesoporous oxides and frameworks.

The systems discussed below include oxide–semiconductor interfaces and proposed Z-scheme or S-scheme arrangements, grouped according to their components and architecture. Band alignment and interfacial contact influence the transfer of photogenerated carriers and the availability of electrons for Cr(VI) reduction. Characterisation of these interfaces is particularly important when assigning a specific pathway, since an increase in removal efficiency cannot, by itself, distinguish between different charge transfer mechanisms.

(a) Narrow-bandgap semiconductors coupled with TiO_2

Alsheheri et al. [19] formed a photoactive p-n junction by decorating mesoporous titanium dioxide (TiO_2) with ZnSe nanoparticles. The incorporation of ZnSe enhanced visible-light absorption and decreased the optical band gap from 3.14 eV for pristine TiO_2 to

2.90 eV for the composite [19]. This TiO_2-ZnSe composite, when prepared with an optimised 3 wt% of ZnSe, could completely reduce 150 ppm Cr(VI) to Cr(III) within 1 h using visible light. The photoreduction rate for the ZnSe-TiO_2 composite was 177 μmol min^{-1}, which exceeded the rates obtained using TiO_2 or ZnSe alone or their physical mixture. During 5 consecutive cycles, the ZnSe-TiO_2 composite retained high photocatalytic activity [19].

Other TiO_2 heterojunctions reported in the literature include bismuth tungstate (Bi_2WO_6)/TiO_2 nanotubes from Wang et al. [45], BiOBr nanoplates anchored onto titanium dioxide (TiO_2) nanorods produced by Xue et al. [46], indium sulphide (In_2S_3)-TiO_2 nanosheets grown on TiO_2 nanofibers produced by Zhang et al. [47], as well as yolk-shell tin disulphide (SnS_2)-TiO_2 produced by Wang et al. [48]. Other TiO_2-based systems, such as TiO_2–ZrO_2 composites, have demonstrated dual functionality. Yan et al. [18] reported simultaneous Cr(VI) photoreduction and Cu(II) removal from wastewater, underscoring the effectiveness of oxide-based TiO_2 composites for heavy-metal remediation.

In addition to the ZnSe nanoparticle-TiO_2 system discussed above, TiO_2 can be coupled with graphitic carbon nitride (g-C_3N_4), which has an energy band gap of approximately 2.7 eV. This produces a heterojunction with interfacial charge transfer depending on the band alignment and contact between g-C_3N_4 and TiO_2, which can promote Cr(VI) reduction and organic pollutant oxidation by facilitating electron–hole separation [49,50]. Related dual-function nitrogen-doped Bi_2O_3/g-C_3N_4 composites were investigated by Khazaee et al. [51] for Cr(VI) photoreduction and RhB photooxidation.

Further g-C_3N_4-based heterojunctions include composites with nickel cobalt layered double hydroxides (NiCo-LDH) by Zhang et al. [52] and zinc ferrite ($ZnFe_2O_4$) by Patnaik et al. [53], as well as graphene oxide/g-C_3N_4/molybdenum disulphide (MoS_2) composites examined by Wu et al. [54].

(b) Bismuth-based oxide photocatalysts and their composites

Bismuth-based semiconductors, including $BiVO_4$, Bi_2WO_6, BiOBr, and BiOI, have attracted considerable interest for photocatalytic Cr(VI) reduction. Their photocatalytic performance depends on their crystal structure, exposed facets, and ability to separate and transfer photogenerated charge carriers. Yu et al. [55] demonstrated the effectiveness of monoclinic $BiVO_4$ with exposed {010} facets for simultaneous Cr(VI) reduction and phenol oxidation. Furthermore, Jia et al. [56] reported that co-doping $BiVO_4$ nanorods with La^{3+} and Gd^{3+} achieved nearly complete Cr(VI) reduction alongside dye decolorization under the reported experimental conditions.

The construction of heterojunctions has further improved the performance of bismuth-based photocatalysts. Liu et al. [57] demonstrated that a hierarchical Bi_2WO_6@CoO Z-scheme heterostructure enabled simultaneous photocatalytic Cr(VI) reduction and tetracycline oxidation under visible light. Its enhanced activity was attributed to efficient charge separation and the preservation of strong redox potentials. Zhao et al. [58] developed a three-dimensional AgI/$BiVO_4$ p–n junction photocatalyst for simultaneous tetracycline oxidation and Cr(VI) reduction. More recently, Sang et al. [59] prepared Bi-MOF-derived porous hierarchical Bi_2O_3/Bi_2S_3 nanoflower-like heterojunctions using a calcination–hydrothermal route for photocatalytic Cr(VI) reduction. These examples illustrate how doping, morphology control, and heterojunction engineering can improve photocatalytic Cr(VI) reduction and, in selected systems, enable its coupling with organic pollutant oxidation.

(c) MXene-Based Photocatalysts

MXenes have attracted increasing interest in Cr(VI) remediation because of their electrical conductivity, reactive surfaces, and ability to participate in adsorption and reduction processes. In semiconductor-based composites, MXenes can facilitate interfacial electron trans-

fer and improve the utilisation of photogenerated charge carriers [5]. Vavilapalli et al. [60] investigated nanocomposites combining brownmillerite $Ca_2Fe_2O_5$ with Ti_3C_2 or $Mo_4/_3C$ MXenes for photocatalytic Cr(VI) reduction to Cr(III) under simulated sunlight. Zhang et al. [61] demonstrated that the structure of $Ti_3C_2T_x$ strongly influenced its adsorption and reduction capabilities, with multilayer and delaminated materials exhibiting different contributions to Cr(VI) removal. Their findings also suggested that $Ti_3C_2T_x/TiO_2$ heterojunctions could enhance the photoresponse and contribute to Cr(VI) reduction.

Other architectures include MXene quantum dots/CuSe n–p plasmonic heterostructures, reported by Yin et al. [62] for rapid photocatalytic Cr(VI) removal under full-spectrum solar irradiation. Separately, Ti_3C_2 MXene/$ZnIn_2S_4$ heterostructures have been investigated by Li et al. [6] for visible-light-driven Cr(VI) reduction. These studies highlight the versatility of MXenes as components of photocatalytic composites. However, adsorption, chemical reduction, and photocatalytic reduction should be distinguished when evaluating their performance, while long-term stability and recyclability require further assessment.

(d) Ternary and multi-component systems

Ternary and multi-component photocatalysts combine semiconductors, cocatalysts, and supporting materials to improve light utilisation, charge transfer, and catalyst recovery. Xu et al. [4] developed a magnetically recoverable $Fe_3O_4/BiVO_4$/CuS heterojunction for simultaneous Cr(VI) reduction and methylene blue degradation under visible light. Other examples include the Bi_2S_3@CdS/rGO S-scheme heterostructure reported by Ghoreishian et al. [63] for photocatalytic Cr(VI) reduction and H_2O_2 production, and the spherical $Bi_2WO_6/Bi_2S_3/MoS_2$ n–p heterojunction investigated by Ren et al. [64] for visible-light-driven Cr(VI) reduction. Patnaik et al. [65] deposited Au–Pd alloy nanoparticles on mesoporous silica-modified g-C_3N_4 for individual and simultaneous phenol oxidation and Cr(VI) reduction. Koutsouroubi et al. [66] also demonstrated photocatalytic Cr(VI) reduction using layered heterostructures comprising Ni-doped MoS_2 and g-C_3N_4.

More complex architectures include the double Z-scheme $FeVO_4/Bi_4O_5Br_2$/BiOBr ternary heterojunction reported by Chachvalvutikul et al. [67] for simultaneous Cr(VI) and Rhodamine B removal. Tu et al. [68] developed an MOF-derived CoS_x@$ZnIn_2S_4/MoS_2$ dual Z-scheme photocatalyst incorporating MoS_2 quantum dots and featuring a hierarchical hollow core–shell structure, further illustrating the structural diversity of multi-component systems.

Supported composites provide an additional approach to combining photocatalytic functions. Aziz et al. [69] investigated silver oxide supported on fibrous silica–zirconia (AgO/FSZr) for simultaneous photocatalytic Cr(VI) reduction and p-cresol oxidation under visible light. Photogenerated electrons were primarily responsible for reducing Cr(VI) to Cr(III), whereas holes and hydroxyl radicals contributed to p-cresol oxidation. The optimised composite was evaluated over five reaction cycles and retained substantial activity, demonstrating its potential for treating mixtures of inorganic and organic pollutants.

Beyond dispersed composites, Wang et al. [70] investigated PVDF-networked CdS/TiO_2 photocatalytic membranes for pharmaceutical wastewater treatment accompanied by Cr(VI) reduction. Such membrane-based systems connect multi-component photocatalyst design with catalyst immobilisation. Overall, these examples highlight complementary strategies for improving photoredox performance and facilitating catalyst recovery, providing a transition to the immobilisation and reactor-design approaches discussed below.

4.4. Catalyst Immobilisation and Reactor Design

Catalyst immobilisation connects material design with practical wastewater treatment by facilitating catalyst retention and reuse while limiting the release of dispersed particles [71]. Magnetic recovery, membrane incorporation, and deposition on solid supports offer different approaches to catalyst management [4,70,72]. Magnetic separation should be distinguished from physical immobilisation. Reactor geometry also affects the distribution of incident light and contact between the solution and photoactive surfaces. Continuous-flow and thin-film configurations may improve these conditions, but their performance depends on catalyst coverage, residence time, and photon delivery. Relevant examples include flat-panel treatment using PVDF-networked CdS/TiO_2 membranes [70] and continuous-flow operation using e-LDH/t-BiOCl/Bi_2S_3 [73]. Immobilisation and reactor design should therefore be evaluated together, including possible losses in accessible surface area or mass-transfer efficiency.

4.5. Real-Water Matrices and Environmental Conditions

Most laboratory studies are conducted under controlled acidic conditions, yet real wastewater may have near-neutral pH and contain competing ions (e.g., sulphate, chloride) and organic co-pollutants. These factors can influence photocatalytic activity and adsorption equilibria [71,74]. Studies using industrial effluents and real-water matrices highlight the need to evaluate photocatalytic performance under realistic water conditions [71,73].

4.6. Catalyst Leaching and Toxicity

Environmental compatibility requires assessment of catalyst integrity as well as Cr(VI) conversion. Metal-containing oxides and framework composites may release constituent ions during operation, depending on their composition and stability in the reaction medium. Dissolved Cr(III) produced by reduction should be distinguished from metals leached from the catalyst, although both are relevant to treated-water quality. Evaluating secondary contamination therefore requires dissolved-metal analysis, repeated-use testing [75], and assessment of residual toxicity. High removal efficiency alone cannot establish that a photocatalyst is suitable for wastewater treatment.

4.7. Life-Cycle and Cost Considerations

Economic feasibility is a key determinant for industrial adoption. High-surface-area mesoporous materials often require complex synthesis routes, increasing cost. Life-cycle assessments should consider raw material availability, synthesis energy demand, catalyst regeneration cycles, and disposal [76]. Comparative cost analyses between conventional treatment methods and photocatalysis will help position mesoporous photocatalysts within practical wastewater management frameworks. Electrical energy consumption is an important consideration, as demonstrated by its optimisation during Cr(VI) photoreduction using immobilised Mg–Ag/TiO_2 [72].

The influence of the water matrix also has an economic dimension. Near-neutral pH, competing ions, and organic co-pollutants can reduce activity relative to model solutions, affecting the treatment performance achievable with a given catalyst. Life-cycle and cost assessments should therefore use performance data obtained under realistic wastewater conditions when evaluating practical treatment scenarios [74,75].

4.8. Scale-Up Feasibility

Scale-up brings these material and process requirements together. Pilot-scale demonstrations remain scarce, and successful operation requires catalyst recovery, control of reactor fouling, and appropriate energy input. Suspended nanoparticles create separation

difficulties and may cause secondary contamination; repeated use can also expose photocorrosion or leaching that is not evident from initial removal efficiency. Immobilisation on supports, magnetic composites, and hybrid systems provide approaches to addressing these recovery and durability constraints [4,72]. Their suitability should be assessed together with reactor geometry and light penetration, rather than from catalyst performance alone. Pilot-scale studies must therefore examine recovery and long-term stability alongside energy demand under industrially relevant conditions. Solar-driven operation and combinations with adsorption or membrane treatment may support practical application, but require evaluation as integrated treatment systems. Such studies would establish how laboratory improvements in activity and reuse translate into sustained wastewater treatment at a larger scale.

5. Cross-Comparison and Critical Analysis

The photocatalysts presented in Section 4 differ in composition, pore architecture, and response to irradiation. Comparing their reported behaviour helps identify the properties associated with Cr(VI) reduction and the conditions under which those properties are useful. Mesoporous TiO_2, ZrO_2, Fe_2O_3, and CoO can be modified by doping or coupling with other phases, while carbon-based frameworks and composites offer additional adsorption and charge transfer pathways. Within the latter group, semiconducting g-C_3N_4 has a different role from conductive graphene or carbon nanotubes. Connected pores in hierarchical core–shell or hollow structures may improve reactant access and light utilisation, but the morphology alone does not establish mesoporosity. Pore-size measurements are therefore needed alongside BET surface area [9]. The results discussed below are considered in relation to these material characteristics and to the experimental conditions. This allows the contribution of pore accessibility to be examined together with surface interactions and carrier behaviour, without assuming that similar removal percentages represent equivalent catalytic activity [2].

5.1. Metal Oxide-Based Photocatalysts

Metal oxides remain widely studied for Cr(VI) photoreduction because their composition and structure can be modified, although their chemical stability depends on composition and reaction conditions. TiO_2, in particular, combines relatively low cost with established activity under UV irradiation [2,16]. Its limited visible-light response and rapid electron–hole recombination account for much of the work on doping and composite formation described in Section 4. The examples below examine how these modifications affect measured reaction rates, surface accessibility, and reuse, beginning with a comparison of commercial TiO_2 samples.

Islam et al. [16] compared AEROXIDE P25, Ishihara Sangyo ST-01, and FUJIFILM Wako TiO_2 nanopowders using formic acid as an electron donor. ST-01 gave the highest apparent pseudo-first-order rate constant and had a surface area of 300 m^2/g and a particle size of 7 nm. P25, however, showed the highest surface-area-normalised rate constant in the same study (Figure 6). The ranking thus changed with the way activity was expressed. A larger surface area was beneficial to the overall treatment rate in this comparison, but did not correspond to the highest rate per unit surface area.

Formic acid enhanced TiO_2-mediated Cr(VI) photoreduction by scavenging holes [16], demonstrating that solution chemistry must be considered together with catalyst structure. Other approaches, including noble-metal loading, oxide–oxide coupling, and metal or non-metal doping, act through changes in interfacial and electronic properties. For the TiO_2–ZrO_2 system, Yan et al. [18] reported that the $Ti_{0.95}Zr_{0.05}$(300) photocatalyst maintained Cr(VI) and Cu(II) removal efficiencies of 100% and 91%, respectively, after

four reaction cycles under UV irradiation using HCOOH–HCOONa as the sacrificial agent. Its pore diameter of 4.5–4.6 nm is consistent with a mesoporous architecture that can support reactant access. However, the reported decrease in surface area after treatment, associated with metal deposition, indicates that initial porosity need not remain accessible during operation. The pre- and post-reaction morphological and crystallographic analyses therefore complement the conversion data by addressing material changes during use [18].

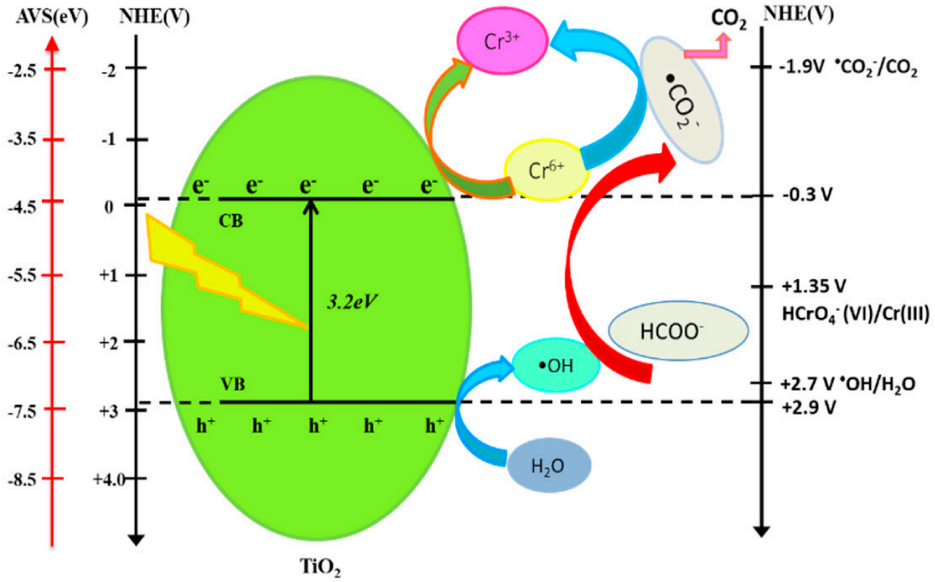


Figure 6. Proposed energy-band and reaction scheme for formic-acid-assisted Cr(VI) reduction over TiO_2, including charge-carrier transfer and surface redox processes. Reproduced from Islam et al. [16].

Hematite (α-Fe_2O_3) absorbs visible light owing to its band gap of approximately 2.2 eV. Du et al. [77] deposited α-Fe_2O_3 on activated microwave-expanded graphite oxide (aMEGO) and reported 95.28% Cr(VI) removal. Their photocurrent and photoluminescence measurements supported improved charge separation in the composite. Sanad et al. [78] instead prepared Fe_2O_3–TiO_2 mixed oxides by hydrothermal–hydrolysis processing, obtaining up to 95.7% Cr(VI) reduction and examining stability and recyclability. The two approaches use different interfaces to modify the behaviour of the oxide phase. Although their endpoint efficiencies are similar, the reaction conditions and the accompanying characterisation are needed to understand the role of the support or second oxide in each system.

Figure 7 compares reported Cr(VI) endpoints for several oxide architectures, whose modifications address different aspects of performance. Ag,Cu-modified WO_3 [79] and TiO_2/$CoFe_2O_4$/Ag [80] incorporate more than one metal component, with the latter also providing magnetic separability. Ni-doped mesoporous CoO assemblies [81] modify the oxide composition within a porous network, whereas CoO/$MnCo_2O_4$ [82] and BiOCl/Bi_2S_3 [83] introduce interfaces between distinct phases. Mesoporous spinel ferrite networks [84] offer a related comparison for the $MnFe_2O_4$–$ZnFe_2O_4$ networks [20], while Bi_2MoO_6/ZnO [85] extends oxide coupling to a bismuth-containing composite. Their reported efficiencies do not isolate the effect of doping, phase coupling, or porosity because irradiation, reaction duration, and solution composition differ. Tests on the individual components under identical conditions and pore measurements are needed to attribute an improvement to a particular design feature.

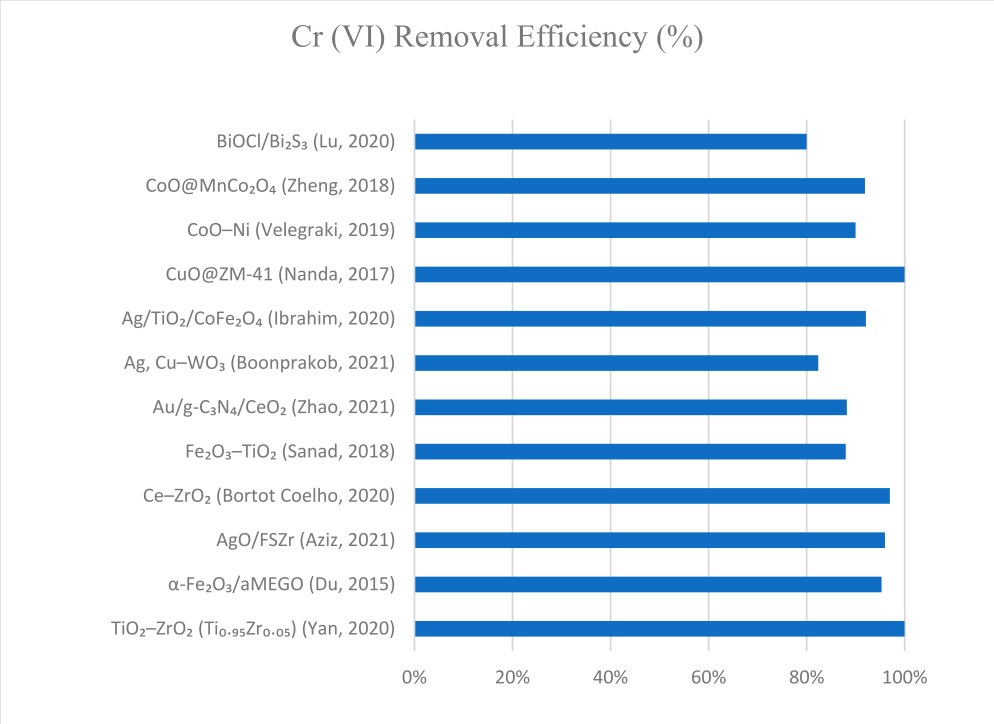


Figure 7. Cr(VI) reduction/removal efficiencies (%) compiled for oxide-based photocatalysts and their composites. The first author's surname and publication year next to each material label identify the source study. Irradiation spectrum and duration, initial Cr(VI) concentration, catalyst loading, pH, electron donors, and co-pollutants differ between studies; the values therefore do not constitute a normalised comparison of intrinsic catalytic activity [17,18,69,71,77–83,86].

5.2. Carbon-Based Photocatalysts and Composites

Graphitic carbon nitride acts as a semiconductor, whereas other carbon components are often used as adsorptive supports or pathways for interfacial electron transfer. Liang et al. [87] examined g-C_3N_4 prepared from different precursors and found the highest Cr(VI) reduction for urea-derived g-C_3N_4 (U-CN): 99.5% in 60 min under white-light irradiation at pH 3 in the presence of citric acid. Its nanosheet morphology, surface area of 81.06 m^2/g, and amine functionality were associated with the enhanced performance. Because these properties changed together with the precursor, the result is best understood in terms of the resulting surface and structure rather than surface area alone.

Hasija et al. [88] discussed g-C_3N_4 for Cr(VI) photoreduction in view of its approximately 2.7 eV band gap, stability, and electronic properties. Coupling with TiO_2, ZnO, or WO_3 can modify its spectral response and introduce interfaces for charge transfer. Measurements on the composite and its individual components are useful here; they help determine whether additional light absorption is accompanied by more effective use of the generated electrons in the reduction reaction.

Wu et al. [54] demonstrated that coupling g-C_3N_4 with GO and MoS_2 to form an intimate heterojunction interface further enhanced its visible-light Cr(VI) photoreduction activity relative to pristine g-C_3N_4. Improved e^-–h^+ separation was supported by the reported measurements, including analysis of the photoluminescence spectra [54].

The composite systems presented in Figure 8 include carbon-containing photocatalysts, such as copper phthalocyanine/rGO [89], $Gd(OH)_3$/rGO [90], SnS_2/g-C_3N_4 [91] and Ni-doped MoS_2/g-C_3N_4 [66], alongside MoS_2/$ZnIn_2S_4$ [92], TiO_2–olive-pit composites [93] and Au/Cu_2O–TiO_2 [94]. These studies examine different combinations of light-absorbing components and interfaces for photocatalytic Cr(VI) treatment. Their reported efficiencies

should be interpreted in relation to the composition of each system and the corresponding irradiation and reaction conditions.

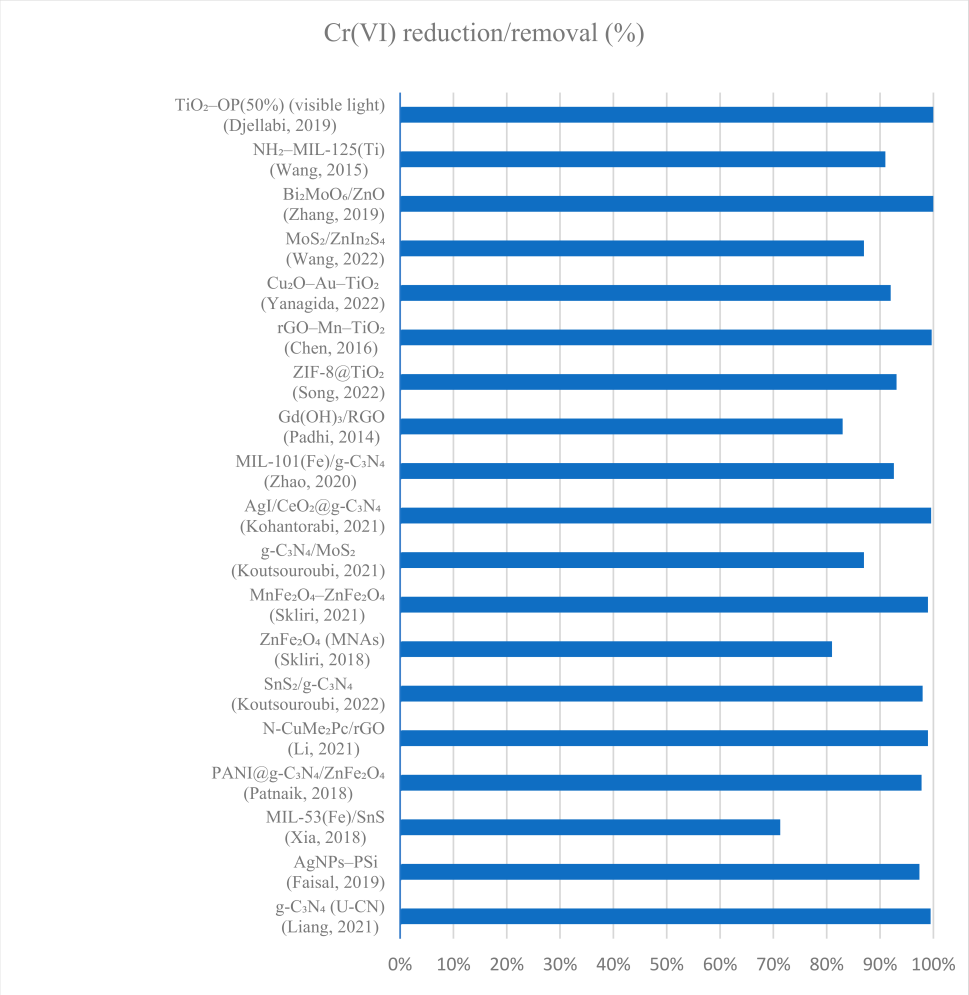


Figure 8. Cr(VI) reduction/removal efficiencies for selected composite systems. The first author's surname and publication year identify the source studies. Reaction time, irradiation, initial concentration, pH, catalyst loading, and electron donors differ between studies, so the bars are not a normalised activity ranking. The 99% bar for [20] summarises a reported >99% endpoint. For rGO–Mn–TiO_2, 99.7% denotes Cr(VI) removal after 60 min of sunlight [95]. In TiO_2–OP(50%), complete Cr(VI) reduction was reported after 50 min of visible-light irradiation; OP denotes olive pits and 50% denotes the sample formulation, not the reduction efficiency [93]. Refs. [7,20,21,53,66,84,85,87,89–99].

Figure 8 summarises the range of reported Cr(VI) reduction/removal endpoints for composite photocatalysts. U-CN reached 99.5% after 60 min under white-light irradiation [87], whereas AgNPs–PSi reached 97.4% after 180 min under visible light [96]. MIL-101(Fe)/g-C_3N_4 achieved 92.6% after 60 min under visible light [21], and AgI/CeO_2@g-C_3N_4 achieved 99.6% after 75 min at pH 3 [97]. The efficiencies presented in Figure 8 were obtained under different experimental conditions, including irradiation, reaction time, initial Cr(VI) concentration, pH, catalyst loading and the presence of electron donors; therefore, they provide an overview of reported performance rather than a direct ranking of photocatalytic activity.

5.3. MOFs and Hybrid Nanocomposites

MOF-based composites allow adsorption and photoinduced charge transfer to be modified within a common architecture, although high porosity alone does not establish

effective Cr(VI) photoreduction. As an oxide-based reference for support and reactor effects, Bortot Coelho et al. [71] examined Ce–ZrO_2 in slurry and immobilised configurations and reported more than 97% Cr(VI) removal from diluted effluent, including humic-acid-containing systems. This example is chemically distinct from MOFs but provides context for evaluating immobilised treatment. Within the MOF family, Zhao et al. [21] reported 92.6% Cr(VI) reduction within 60 min under visible light for MIL-101(Fe)/g-C_3N_4, exceeding either component alone; the enhancement was associated with light absorption and proposed Z-scheme interfacial charge transfer. For comparison, MIL-53(Fe)/SnS and PANI@g-C_3N_4/$ZnFe_2O_4$ are shown in Figure 8 with Cr(VI) reduction/removal efficiencies of 71.3% and 97.8%, respectively [53,98]. Their different material functions and reaction conditions should be considered separately, and the endpoint percentages do not establish an intrinsic activity ranking.

5.4. Noble Metal-Based and Multi-Component Systems

Noble-metal-containing photocatalysts should be assessed according to the chemical form and function of the metal. Ag or Au incorporation can modify interfacial electron transfer and, where demonstrated, introduce plasmonic effects. Aziz et al. [69] investigated AgO/FSZr composites and reported 96% Cr(VI) reduction for the 5-AgO/FSZr sample in coupled Cr(VI)/p-cresol treatment with stable performance over five cycles. Their interpretation involved a reduced band gap and improved charge separation. Catalytic function should therefore be established for the specific composite rather than inferred from the presence of a noble metal.

Multi-component systems provide further examples of combining light absorption, interfacial transport, and pollutant adsorption. Au/g-C_3N_4/CeO_2 [86] achieved Cr(VI) reduction and oxytetracycline hydrochloride oxidation efficiencies of 88.2% and 95.1%, respectively, associated with improved visible-light absorption and electron transfer. Mesoporous $ZnFe_2O_4$–$MnFe_2O_4$ composites [20] exhibited Cr(VI) reduction near 99%, although industrial suitability requires evidence beyond initial conversion. For rGO–Mn–TiO_2, 99.7% Cr(VI) removal was reported after 60 min of sunlight irradiation; the separately reported 99.02% value refers to total chromium removal [95]. Framework-containing systems provide complementary comparisons: ZIF-8@TiO_2 achieved 93.1% removal after 120 min under UV–vis irradiation [99], whereas the NH_2–MIL-125(Ti) study examines visible-light activity and the influence of pH and hole scavengers [7]. The compiled Figure 8 includes a 91% endpoint for NH_2–MIL-125(Ti) [7]. Porous TiO_2/ZIF-8 [100] and TiO_2/MOF-801(Zr) [34] extend this group. These overlapping material categories illustrate why composition, measured chromium species, and experimental conditions must accompany any comparison of efficiency.

5.5. Summary Tables of Mesoporous Photocatalysts

Tables 1 and 2 summarise selected studies on photocatalytic Cr(VI) reduction using metal oxides, noble-metal-containing systems, framework materials, and hybrid composites. The tables compile material characteristics and experimental parameters, including specific surface area, pore size, light source, pH, hole scavengers, initial Cr(VI) concentration, catalyst loading, irradiation wavelength and intensity, reaction time, kinetic rate constants, reusability, and dark adsorption and photolysis controls, where reported. This format facilitates comparison of the reported performance and supporting evidence, although differences in experimental conditions limit direct quantitative comparisons between photocatalysts.

Table 1. Selected metal oxide and hybrid photocatalysts for Cr(VI) reduction.

Ref.	Material	SSA/Pore Size	Cr(VI) Removal/Reduction (%)	Light Source	pH	Hole Scavenger/Organic Co-Substrate	Key Features	Cr(VI) Conc. (mg/L)	Catalyst Loading (g/L)	Wavelength/Irradiance	Irradiation Time	Rate Constant, k (min^{-1})/Kinetic Ratio	Stability/Reusability	Controls (Dark/Photolysis)
[16]	TiO_2 (ST-01, P25, FUJIFILM)	ST-01: 300 m^2 g^{-1}; P25: 50 m^2 g^{-1}; FUJIFILM: 8.7 m^2 g^{-1}	≈98% (P25)	UV black-light (lamp 15 W)	3	Formic acid (0.30%)	Large specific surface area; formic acid promotes Cr(VI) photoreduction	30	0.67	λmax ≈ 352 nm (emission peak); 0.25 mW cm^{-2}	120 min	ST-01: 0.087; P25: 0.043; FUJIFILM: 0.0031	NR	30 min dark equilibration; illuminated tests without TiO_2
[18]	TiO_2–ZrO_2, $Ti_{0.95}Zr_{0.05}$(300)	166.5 m^2 g^{-1}/ ~4.5 nm	100% (complete Cr(VI) removal)	UV light	3	HCOOH–HCOONa (1 ml per 20 ml solution)	Removal of coexisting Cr(VI) and Cu(II) by photoreduction	20	3	365 nm	60 min	0.041	4 cycles; 100% Cr(VI) and 91% Cu(II) removal after the fourth cycle	25% total Cr removal in the dark (60 min)
[77]	α-Fe_2O_3/aMEGO (7.72 wt% aMEGO)	120.5 m^2 g^{-1}/ NR	95.28% (vs. 25.26% for pristine α-Fe_2O_3)	300 W xenon lamp	2	None added	Conductive carbon support facilitates electron transport and suppresses charge-carrier recombination	10	1	λ > 420 nm (cut-off)	160 min	0.01829	93.02% reduction after 3 cycles	Dark control, 30 min
[69]	5-AgO/FSZr	256 m^2 g^{-1}/7.91 nm	96% Cr(VI) reduction; 78% p-cresol oxidation	36 W metal halide lamp	1	p-Cresol (10 mg L^{-1})	Coupled Cr(VI) reduction and p-cresol oxidation; suppressed charge-carrier recombination	10	0.4	λ = 400 nm	180 min	0.029	5 cycles, 92% retained efficiency	Dark control, 3% Cr(VI) removal
[98]	MIL-53(Fe)/SnS (MS-15; prepared with 15 mg MIL-53(Fe))	33.965 m^2 g^{-1} (MS-15)	71.3% (photoreduction)	300 W xenon lamp	NR	None added	Enhanced visible-light absorption and charge separation; k ≈ 7.5 × that of pristine MIL-53(Fe) and ≈5.2 × that of pristine SnS	20	1	λ > 420 nm (long-pass cut-off filter)	60 min	0.01878	5 cycles; Cr(VI) reduction: 71.7% initially → 65.9% after reuse	60 min dark adsorption–desorption equilibration
[78]	Fe_2O_3–TiO_2 (1:1)	107–204 m^2 g^{-1}	95.7%	150 W xenon arc lamp; 1000 W halogen lamp (visible)	3.9–4	None added	Cr(VI) photoreduction under UV and visible-light irradiation	10	2	NR	360 min	NR	5 cycles, 3.7% activity loss	30 min dark adsorption–desorption equilibration

Note: Rate constants are in min^{-1}; kinetic ratios are dimensionless. Conditions and endpoints differ between studies. Lamp power (W) is distinct from irradiance (mW cm^{-2}). λmax denotes an emission peak; a long-pass cut-off denotes transmitted longer wavelengths. SSA: specific surface area; NR: not reported in the main article.

Table 2. Selected framework-based and bismuth-based photocatalysts for Cr(VI) reduction.

Ref.	Material	SSA/Pore Size	Cr(VI) Removal/Reduction (%)	Light Source	pH	Hole Scavenger/Organic Co-Substrate	Key Features	Cr(VI) Conc. (mg/L)	Catalyst Loading (g/L)	Wavelength/Irradiance	Irradiation Time	Rate Constant, k (min^{-1})/Kinetic Ratio	Stability/Reusability	Controls
[36]	NH_2-MIL-101(Fe)/$ZnIn_2S_4$ (optimal 10% formulation)	70.08 m^2 g^{-1}/11.01 nm	94%	300 W Xe lamp	7	None added	0D/3D heterojunction with proposed S-scheme charge transfer; separate Cr(VI) reduction and photo-Fenton-like 2-nitrophenol degradation tests	20	0.2	$\lambda > 420$ nm	60 min	0.0431	4 cycles: efficiency decrease from 94% to 85%	Dark + photolysis
[33]	Halogen-functionalized COFs (TAPP-2F, TAPP-2Cl, TAPP-2Br)	454.45 m^2 g^{-1} (TAPP-2F)	~100% (TAPP-2F); lower for Cl/Br	300 W Xe lamp	3	None added	Halogen substitution tunes band structure and enhances charge-carrier separation	5	0.2	$420 \leq \lambda \leq 780$ nm (irradiation range)	120 min	Highest for TAPP-2F, 0.22 (TAPP-2F), O.017 (TAP-2Cl), 0.013 (TAPP-2Br)	5 cycles: nearly 100% (TAPP-2F)	Dark + photolysis
[55]	Monoclinic $BiVO_4$ ({010}-oriented)	NR	~100%	300 W Xe lamp	<1	Phenol (50 mg L^{-1})	Facet-dependent charge separation and transfer associated with {010}-oriented growth	8	1	$\lambda > 420$ nm (cut off filter)	150 min	NR	NR	Dark + photolysis
[12]	Bi_2S_3–$BiVO_4$ graphene aerogel (3D Z-scheme)	NR	Nearly 100% Cr(VI) and BPA removal (adsorption + photocatalysis)	300 W Xe lamp	2	BPA (10 mg L^{-1})	Adsorption coupled with photocatalysis; proposed Z-scheme charge transfer	50	0.8	$\lambda > 420$ nm (cut off filter)	120 min irradiation after 40 min dark adsorption	NR	5 cycles: >85% removal both Cr(VI) and BPA	Dark + photolysis

Note: Rate constants are in min^{-1}; kinetic ratios are dimensionless. Conditions and endpoints differ between studies. Lamp power (W) is distinct from irradiance (mW cm^{-2}). λmax denotes an emission peak; a long-pass cut-off denotes transmitted longer wavelengths. SSA: specific surface area; NR: not reported in the main article; BPA: bisphenol A.

Reporting Parameters and Comparability of Studies

The parameters in Tables 1 and 2 provide a common reporting framework for studies conducted under different experimental conditions. Initial Cr(VI) concentration, catalyst loading, irradiation wavelength/intensity, pH, hole scavengers, and co-pollutants define the reaction environment in which each efficiency was obtained. Kinetic constants, reusability, and control experiments (dark adsorption and photolysis) provide complementary information about reaction progress, durability, and removal mechanisms. Where a parameter was absent from the original publication, the corresponding entry is marked as 'not reported.' Reading these descriptors together allows differences in reported efficiencies to be interpreted in context while avoiding a direct ranking of systems tested under dissimilar conditions.

5.6. Summary and Critical Analysis

Cr(VI) photoreduction efficiencies above 90% are common in the reviewed studies, although lower values are also reported. Some systems approach complete removal within 30–60 min under optimised conditions [18,33,36]. Tables 1 and 2 show that these results have been obtained with different combinations of accessible surface area, surface functionality, visible-light response, and interfacial charge transfer. Selected oxides offer useful stability and reuse characteristics; carbon-based and MOF composites provide additional options for modifying spectral response and charge transport [77,98]. The advantages vary among individual materials, while differences in experimental conditions prevent a definitive ranking of the material classes. Activity near neutral pH and retention of conversion during reuse are particularly relevant when considering wastewater applications. In this respect, a catalyst that combines adequate conversion with stable operation may be more useful than one that achieves a higher initial percentage only under demanding reaction conditions. The comparison therefore depends on both treatment performance and the requirements for maintaining it.

The experimental differences are substantial: reported solution pH values range from strongly acidic conditions to neutral conditions [16,36,69], and irradiation includes UV, visible light, and sunlight. Electron donors and organic co-pollutants also affect the supply of electrons available for Cr(VI) reduction. Islam et al. [16], for instance, used formic acid to consume holes during TiO_2 photocatalysis. Some donor-free systems required longer irradiation to reach high endpoint removal. Their slower conversion cannot be attributed to the catalyst alone, since the oxidation reaction and solution composition also differ. Comparing these systems requires attention to donor addition, pH, and irradiation as well as to catalyst composition and pore structure.

A further limitation is the emphasis on initial conversion in controlled model solutions rather than sustained operation in realistic water matrices. Acidic conditions and lower initial Cr(VI) concentrations can favour higher percentage removal, but their effects depend on surface charge, chromium speciation, and the availability of reactive sites. At high Cr(VI) concentrations or in the presence of competing ions, changes in adsorption and site accessibility can alter the apparent performance. Pore blockage, surface deposition, and loss of selectivity should therefore be treated as mechanisms requiring experimental evaluation rather than inferred solely from a decline in efficiency. Repeated-use measurements under representative wastewater conditions are needed to connect initial textural properties with durability during treatment.

Endpoint removal remains the most widely reported measure, while kinetic data, chromium speciation, and mechanistic characterisation are less consistently available. Photoluminescence and photocurrent measurements, such as those used for α-Fe_2O_3/aMEGO [77], provide information on carrier behaviour. Dark adsorption and photolysis controls help

distinguish adsorption and direct photolysis from photocatalytic removal, while chromium speciation analysis is needed to confirm Cr(VI) reduction to Cr(III). These measurements answer different questions and are most informative when reported together. The literature supports further development of mesoporous photocatalysts, but separating the effects of pores, surface chemistry, and electronic structure still requires suitable reference materials. The practical challenges in Section 6 follow from this need to establish both the mechanism of removal and the durability of the treatment under realistic conditions.

5.7. Comparative Synthesis of Additional Photocatalytic Systems

The additional studies on photocatalytic Cr(VI) reduction can be compared according to the function of the modification and the evidence used to assess it. Carbon quantum dots [101], phthalocyanines [102] and polydopamine [103] introduce light-responsive surface components into TiO_2-based systems, whereas Mo doping [104] and N doping [105] modify the oxide itself. The study of pristine TiO_2 under visible irradiation [106] provides a complementary reference for examining how the pollutant and solution composition participate in electron transfer. These approaches address different limitations of TiO_2; their effectiveness should therefore be judged against the corresponding unmodified material under the same illumination and solution conditions. A broader absorption spectrum alone does not establish that the absorbed photons drive Cr(VI) reduction.

Oxide coupling can also modify adsorption and the distribution of reactive sites. Studies of Bi_2O_3/TiO_2 with bisphenol A [107], TiO_2/hydroniumjarosite [108], Cu–TiO_2/CuO [109], and CdS/ZnAlO [110] examine different combinations of light absorption and redox functions. Zn–Al layered double hydroxide/TiO_2 [111] and $CuCo_2O_4/TiO_2$ [112] explicitly connect adsorption with photocatalytic treatment, making dark equilibration and chromium mass balances central to interpretation. Kaur et al. [113] reported a BJH pore diameter of 3.64 nm for TiO_2–Al_2O_3–$ZnFe_2O_4$, providing sample-specific evidence of mesoporosity. In contrast, surface morphology alone cannot establish a 2–50 nm pore population. For $ZnFe_2O_4$-decorated Al_2O_3/MCM-41, Das et al. [114] reported 66% Cr(VI) reduction after 60 min under sunlight; the separate 99% phenol result after 40 min should not be assigned to chromium. These examples illustrate why both pore descriptors and pollutant-specific endpoints are needed.

Sulphide-containing heterostructures offer several routes to visible-light activity. $MgIn_2S_4$/CdS [115] combines Cr(VI) photoreduction with a separate hydrogen-evolution application. UCNPs@$Zn_xCd_{1-x}S/TiO_2$ yolk–shell nanoparticles [116], incorporating an amorphous TiO_2 layer, were investigated for Cr(VI) photoreduction under near-infrared and simulated solar irradiation. The proposed charge transfer pathways in vacancy-modified MoS_2/SnS_2 [117], chemically bonded $Mn_{0.5}Cd_{0.5}S$/BiOBr [11], and e-LDH/t-BiOCl/Bi_2S_3 [73] should be assessed in relation to their respective interfaces and operating conditions. WS_2/BiOBr [118], black phosphorus/P-doped BiOCl [119], TiO_2/BiOCl [120], and oxygen-vacancy-rich $TiO_2/Bi_4O_5Br_2$ [121] extend this comparison to bismuth-based junctions. $ZnIn_2S_4/In_2O_3$ nanofibers [122], SnS_2/TiO_2 [123], and $LaNiO_3$/g-C_3N_4/MoS_2 [124] use different contact geometries and component functions. Together, these studies support examination of interfacial transport, but the terms Z-scheme and S-scheme should remain tied to the evidence reported for each system rather than inferred from improved removal alone.

Carbon-containing systems likewise require a distinction between the photoactive phase and the role of the carbon component. Carbon dot–silica hybrids [125] combine Cr(VI) adsorption with a visible-light response, while catechol–TiO_2 carbonaceous polymers [126] modify the organic–inorganic interface. Graphitic carbon nitride/titania mesoflowers [49] provide a related adsorption example: their reported Cr(VI) removal

concerns sorption, whereas photocatalytic activity was evaluated for organic contaminants. The g-C_3N_4/Fe-ZnO/RGO [127] and metal-free graphene/g-C_3N_4/carbon-dot heterostructures [128] provide further examples of carbon-containing composite architectures. The study by Zong et al. [50], which tested urea-modified TiO_2 under visible, UV, and simulated solar irradiation, is useful for examining how preparation and illumination affect the interpretation of a carbon-nitride modification. These comparisons require controls for each component and for adsorption, because the presence of carbon, an increased BET area and a higher removal percentage do not independently demonstrate the same enhancement mechanism.

Framework and polyoxometalate composites illustrate how interfacial design can be combined with selective surface interactions. UiO-66-NH_2/$ZnIn_2S_4$ [129] and MIL-68(Fe) [130] address Cr(VI) treatment with different framework chemistries, whereas polyoxometalate/TiO_2/Ag nanofibers [131], CdS/$Cs_3PW_{12}O_{40}$ [132], and calcined ZnTi-layered double hydroxide containing PW_{12} units [133] introduce redox-active polyoxometalates. $Bi_3O(PO_4)_2(OH)$/$BiPO_4$ [134] and Bi_2MoO_6/Bi_2S_3 [135] explicitly combine adsorption and photoreduction. Fu et al. [136] provide an informative mixed-pollutant example: MIL-125-NH_2@$BiVO_4$ removed 41.0% Cr(VI), compared with 98.7% malachite green and 99.1% methylene blue in the ternary mixture after 3 h in a neutral medium. In the same ternary pollutant system, Cr(VI) removal reached 57.1% after 3 h at pH approximately 2 [136], illustrating the influence of solution conditions. The distinct endpoints show that efficient dye removal cannot be used as a proxy for chromium conversion. Framework identity also does not, by itself, establish the mesoporosity of the tested composite.

Metal incorporation should be compared through its chemical form and location. Bi/Bi_2WO_6 [137] uses a non-noble metal component, while the TiO_2@Au@CeO_2 study [138] examines Cr(VI) photoreduction while varying the position of Au within a hollow composite. Cu/TiO_2 nanorods [139] provide another metal–semiconductor interface for combined dye and Cr(VI) treatment. These examples concern different interfacial arrangements; attributing their behaviour solely to the presence of a metal would overlook the roles of contact geometry and the oxidation reaction. Within-study comparisons of metal placement or loading are therefore more informative for establishing a cocatalyst effect than comparisons between endpoint percentages taken from separate publications.

Immobilised and recoverable systems shift the comparison from powder activity to catalyst retention and reactor operation. Porous TiO_2 coatings [140], plasma-electrolytic-oxidation coatings [141], and anodic TiO_2 nanotubes [142] retain the catalyst on a substrate; silver-containing titania on waste-derived polystyrene [143], floating mesoporous TiO_2/polyurethane composites [144], and transparent PVA/TiO_2 films [145] use other support configurations. SnS_2/nickel–sulphide junctions on nickel foam [146], $FeCl_3$- and TiO_2-treated algae [147], and magnetic TiO_2–lignocellulosic biomass/Fe_3O_4 [148] further diversify the recovery strategies. Ultrafiltration photocatalytic membranes [149] and sulphonated-polysulphone/TiO_2 membranes [150] additionally combine separation with treatment. Membrane rejection, adsorption, and photoreduction must be resolved as distinct contributions. In the PEO study [141], morphology and porosity were evaluated qualitatively, so the coating should not be classified as quantitatively confirmed mesoporous on that basis. These configurations also require reporting of exposed area, residence time or flux, and catalyst loss during reuse.

Operating conditions can change the apparent benefit of the same material. Machado et al. [151] compared photochemical and TiO_2-mediated routes in the presence of ethanol, providing a basis for distinguishing direct photochemistry from heterogeneous photocatalysis. Chang and Wu [152] reported rate constants of 0.260 and 0.038 min^{-1} for Ag/Fe_3O_4/TiO_2 nanofibers with and without ammonium oxalate, respectively; this within-study compar-

ison demonstrates why electron-donor conditions must accompany kinetic values. The formate-mediated $CO_2^{\bullet-}$ process in leather wastewater [153] similarly depends on solution chemistry, while the plating-wastewater study [154] examines pH and catalyst concentration. Carbon-quantum-dot/CdS nanosheets were evaluated under saline conditions [74], and e-LDH/t-BiOCl/Bi_2S_3 was also examined in real-water and continuous-flow settings [73]. Energy consumption was explicitly considered for immobilised Mg,Ag/TiO_2 [72], whereas a photocatalytic fuel cell coupled pollutant removal with electricity generation [155]. These studies broaden practical assessment beyond conversion, but their reactor and matrix conditions must remain identifiable when comparing performance.

The synthesis above distinguishes Cr(VI)-specific evidence from related photocatalytic background. In the TiO_2/oxidant study [156], Cr(VI) was added to promote acid orange 7 (AO7) degradation under simulated solar irradiation. The authors also reported that nearly 60% of Cr(VI) was photocatalytically reduced to Cr(III), making this a coupled oxidation–reduction example. The chromium-reduction result must be distinguished from the dye-degradation efficiency. The H_2- and H_2O_2-production studies [13–15] provide interfacial-design context rather than chromium-treatment data.

Together with the studies discussed in the preceding sections and summarised in Tables 1 and 2, these findings inform the comparative assessment of photocatalytic Cr(VI) reduction. Background literature supports the discussion of material design and reaction mechanisms and is distinguished from the experimental studies included in the screening procedure described in Section 2.

6. Practical Challenges

6.1. Catalyst Recovery

Recovering nanoscale photocatalysts from treated waters presents a significant practical barrier. Centrifugation and filtration can require substantial energy input and may be inefficient for processing large volumes of treated wastewater. Magnetic composites incorporating Fe_3O_4 can facilitate catalyst separation from treated water using an external magnetic field [4,148]. Further research should assess the long-term stability of magnetic composites during photocatalytic treatment, including possible particle release and changes in catalyst recovery efficiency over repeated cycles.

6.2. Metal Leaching and Secondary Contamination

Some photocatalysts contain potentially hazardous metals, particularly cadmium in CdS-based systems, such as Bi_2S_3@CdS@RGO [63]. Metal-ion leaching during treatment can cause secondary contamination and should therefore be evaluated under the relevant operating conditions. Cd-free alternatives include TiO_2- and g-C_3N_4-based systems [16,87], as well as selected Fe-based materials [77], although their environmental compatibility should not be assumed solely from their composition. Assessment should include dissolved-metal measurements and residual-toxicity testing, together with stability evaluation over repeated treatment cycles.

6.3. Real Wastewater Matrices

Many laboratory studies use synthetic Cr(VI) solutions prepared in deionized water. However, actual industrial wastewater may present additional matrix-related factors:

i. Coexisting ions, such as chloride, sulphate, phosphate, Ca^{2+}, and Mg^{2+}, may alter adsorption and reaction pathways depending on their identity and concentration.

ii. Organic co-pollutants, such as dyes, phenols, and antibiotics, may promote Cr(VI) photoreduction by consuming photogenerated holes [11,106] or inhibit treatment through competitive adsorption and light screening.
iii. Variable solution pH affects chromium speciation, catalyst surface charge, and the thermodynamic driving force for Cr(VI) reduction [7,154].
iv. Elevated ionic strength may affect adsorption, particle aggregation, and catalyst dispersion.

Because relatively few studies have examined actual wastewater, these matrix effects remain an important gap in the evidence for practical application. Future testing should therefore prioritise realistic wastewater conditions.

6.4. Scalability and Reactor Design

Scaling up photocatalytic Cr(VI) reduction from laboratory experiments to practical treatment applications requires consideration of both catalyst production and reactor operation. Key considerations for scale-up include:

i. Low-cost, readily available precursors and reduced reliance on noble metals, where suitable alternatives are available.
ii. Reproducible synthesis methods with limited processing steps, solvent consumption, and energy requirements are needed. One-pot and template-free approaches may simplify production, whereas hydrothermal and solvothermal methods require evaluation of their temperature, pressure, and equipment requirements.
iii. Catalyst immobilisation on supports, such as fibres, membranes, or foams [140,146,149], facilitates recovery and reuse, while accounting for possible limitations in accessible surface area and mass transfer.
iv. Photoreactor designs should provide effective light distribution, adequate contact between Cr(VI) and the catalyst, and sufficient residence time. Continuous-flow configurations [73] warrant investigation for sustained treatment, alongside suitable slurry and immobilised-catalyst systems.

The suitability of these approaches should be assessed through pilot-scale testing under realistic wastewater conditions. Evaluation should include Cr(VI) reduction efficiency, catalyst stability and reuse, energy consumption, and treatment throughput.

6.5. Cost Considerations

Noble-metal incorporation may improve photocatalytic performance, but it also adds to catalyst production costs. Its economic justification therefore depends on the metal loading and the resulting gains in Cr(VI) reduction activity, catalyst lifetime, and reuse. Catalysts based on more abundant metals, such as Fe, Mn, or Cu, may offer lower-cost alternatives, provided that their performance, stability, and potential metal leaching are adequately assessed.

Economic evaluation should consider precursor costs, synthesis and immobilisation requirements, reactor investment, energy consumption for irradiation and pumping [72], and any required chemical additives. Catalyst recovery, regeneration, replacement, and the management of chromium-containing residuals should also be included. Comparisons should be made under comparable treatment conditions and expressed in terms of cost per unit volume of water treated to a specified residual Cr(VI) concentration.

6.6. Standardisation of Performance Metrics

Recent studies of MXenes, COFs, S-scheme heterojunctions, and photocatalytic membranes during 2024–2026 have broadened the range of architectures investigated for Cr(VI) reduction. Examples include NH_2-MIL-101(Fe)/$ZnIn_2S_4$ [36], defect-engineered

MOFs [37], halogen-functionalized COFs [33], MXene-based composites [5], and photocatalytic membranes [70]. Evaluating these developments requires consistent reporting as well as material innovation. Catalyst immobilisation and reactor design, performance in real-water matrices, leaching and toxicity tests, life-cycle and cost analyses, and scale-up conditions describe complementary aspects of practical suitability. These aspects should be considered alongside removal efficiency when interpreting new materials, so that laboratory advances can be assessed against the requirements of wastewater treatment rather than solely against endpoint percentages.

Differences in testing conditions and reporting practices continue to limit reliable cross-study comparisons. A minimum reporting standard should include:

- Initial Cr(VI) concentration (mg L^{-1});
- Catalyst loading (g/L);
- Light source characteristics (lamp type, wavelength range and filters, irradiance at the reactor, and source-to-reactor distance);
- pH of the solution;
- Presence and concentration of any hole scavenger;
- Dark controls to assess adsorption and any non-photochemical Cr(VI) reduction;
- Catalyst-free irradiation controls to assess direct photochemical Cr(VI) reduction;
- Time-resolved Cr(VI) concentration data and, where justified, apparent kinetic rate constants, including the fitting model, units, and goodness of fit;
- Reusability data (multiple cycles with activity retention percentage);
- Irradiation time, solution volume, and reaction temperature;
- Water matrix composition, including relevant coexisting ions and organic co-pollutants;
- Analytical methods for Cr(VI), evidence of Cr(III) formation, and chromium mass balance where feasible;
- Replicate measurements and experimental uncertainty.

Adopting a common reporting standard would make the practical questions discussed above easier to evaluate across studies. Defined irradiation conditions and kinetic data support interpretation of reaction performance; adsorption and photolysis controls clarify removal mechanisms; and reuse measurements provide context for catalyst durability. These measurements also supply the basis for evaluating immobilisation, reactor design, and operation in realistic water matrices. Leaching and toxicity assessments, together with life-cycle and cost analyses, remain necessary to determine whether improved laboratory performance supports practical implementation. The value of standardisation is therefore to connect material development with reproducible assessment of treatment performance and the evidence required for scale-up, rather than to treat a single removal percentage as a measure of overall suitability.

For manufacturing, the central difficulty is reproducing the material properties responsible for laboratory performance at larger production volumes. Complex templating and calcination routes can increase costs, while maintaining uniform pore structures and stability under variable water chemistries remains challenging. These constraints link synthesis reproducibility with treatment reliability and should inform comparisons with conventional adsorbents and reductants. Economic viability must be assessed alongside photocatalytic performance under the relevant operating conditions. Establishing this connection between reproducible manufacture, stable operation, and cost-effectiveness is necessary before mesoporous materials can progress from laboratory demonstrations to commercially viable wastewater treatment technologies.

7. Conclusions and Future Directions

Mesoporous materials offer several ways to improve photocatalytic Cr(VI) reduction. Accessible surfaces favour contact with chromium oxyanions, connected pores facilitate reactant transport, and the incorporation of dopants or additional phases can modify light absorption and charge transfer. Selected systems have shown improved Cr(VI) reduction relative to their corresponding controls, with some approaching complete conversion under the specific experimental conditions reported. The benefit of mesoporosity depends on the surrounding chemical and electronic structure, rather than pore size alone. Pore characterisation and reaction controls remain necessary for identifying that contribution in each material. The results reviewed here favour designs in which accessible pores and suitable surface chemistry work together with effective utilisation of photogenerated electrons.

High Cr(VI) reduction efficiencies have been reported under acidic conditions, with sacrificial electron donors and/or cocatalysts used in some systems. Apparent pseudo-first-order kinetics are frequently used to describe the reaction, although the fitted rate constants depend on concentration, irradiation, and the interval considered. Comparisons with less porous controls are consequently most useful within experiments conducted under equivalent conditions. Operating limits also need attention. Catalyst loading above a system-specific optimum may increase light attenuation, while high initial Cr(VI) concentrations can saturate accessible sites and lower the apparent rate. Material development must therefore be accompanied by optimisation of the reaction conditions. Further work should establish whether the resulting performance can be maintained during wastewater treatment, where water composition and operating demands are less readily controlled.

A primary direction is to scale up selected mesoporous photocatalysts and test them under realistic wastewater conditions, examining the effects of competing ions and catalyst instability over extended reuse cycles. Secondly, efforts towards pore structure modification and functionalization tailored for Cr(VI) capture and photoreduction should continue. Further development of MOF- and COF-based systems should establish how their measured pore structures and surface functionalities contribute to Cr(VI) adsorption and photoreduction. Thirdly, standardisation of performance evaluation criteria and protocols should be encouraged in future research to facilitate comparison between different catalysts and experiments. This would involve measuring contaminant removal at defined time intervals and reporting kinetic data under comparable irradiation and pH conditions. Lastly, detailed mechanistic studies using advanced spectroscopic methods and theoretical models could clarify how mesoporosity affects the electron–hole dynamics involved in Cr(VI) reduction.

These research directions can be brought together through three complementary design priorities. Pore engineering should connect hierarchical mesoporous structures and tailored surface functionalization with pollutant diffusion, adsorption selectivity, and photon utilisation. Multifunctional catalyst design should examine how photocatalysis interacts with adsorption, advanced oxidation, or membrane separation in complex wastewater matrices, including the consequences for catalyst stability. System development should then evaluate immobilised films, membrane-based composites, and continuous-flow reactors as means of implementing these material functions at a practical scale. Considering pore structure, combined treatment functions, and reactor configuration together provides a coherent route for testing whether mesoporous photocatalysts can deliver sustained and sustainable Cr(VI) remediation beyond the laboratory.

Author Contributions: Conceptualisation and supervision, I.T.P. and S.A.C.; writing—original draft preparation, E.B. and I.T.P.; interpretation of the reviewed literature concerning light absorption, charge-carrier separation and transfer, and photocatalytic mechanisms of Cr(VI) reduction, A.I.; writing—review and editing, I.T.P., S.A.C., and A.I. All authors have read and agreed to the published version of the manuscript.

Funding: This research received no external funding.

Institutional Review Board Statement: Not applicable.

Informed Consent Statement: Not applicable.

Data Availability Statement: The original contributions presented in this study are included in the article. Further inquiries can be directed to the corresponding author.

Conflicts of Interest: The authors declare no conflicts of interest.

References

1. Wang, C.C.; Du, X.D.; Li, J.; Guo, X.X.; Wang, P.; Zhang, J. Photocatalytic Cr(VI) reduction in metal-organic frameworks: A mini-review. *Appl. Catal. B Environ.* **2016**, *193*, 198–216. [CrossRef]
2. Zhang, T.; Wang, P.; Li, Y.; Bao, Y.; Lim, T.T.; Zhan, S. Advances in dual-functional photocatalysis for simultaneous reduction of hexavalent chromium and oxidation of organics in wastewater. *Environ. Funct. Mater.* **2023**, *2*, 58–69. [CrossRef]
3. UN-Water; UNESCO. *United Nations World Water Development Report 2020: Water and Climate Change*; UNESCO: Paris, France, 2020.
4. Xu, G.; Du, M.; Zhang, J.; Li, T.; Guan, Y.; Guo, C. Facile fabrication of magnetically recyclable Fe_3O_4/$BiVO_4$/CuS heterojunction photocatalyst for boosting simultaneous Cr(VI) reduction and methylene blue degradation. *J. Alloys Compd.* **2022**, *895*, 162631. [CrossRef]
5. Fattah-alhosseini, A.; Sangarimotlagh, Z.; Dikici, B.; Kaseem, M. MXene-based composites for enhanced photocatalytic Cr(VI) removal in wastewater: A comprehensive review. *J. Alloys Compd.* **2025**, *1015*, 178846. [CrossRef]
6. Li, S.; Shao, L.; Yang, Z.; Cheng, S.; Yang, C.; Liu, Y.; Xia, X. Constructing Ti_3C_2 MXene/$ZnIn_2S_4$ heterostructure as a Schottky catalyst for photocatalytic environmental remediation. *Green Energy Environ.* **2022**, *7*, 246–256. [CrossRef]
7. Wang, H.; Yuan, X.; Wu, Y.; Zeng, G.; Chen, X.; Leng, L.; Wu, Z.; Jiang, L.; Li, H. Facile synthesis of amino-functionalized titanium metal-organic frameworks and their superior visible-light photocatalytic activity for Cr(VI) reduction. *J. Hazard. Mater.* **2015**, *286*, 187–194. [CrossRef] [PubMed]
8. Shen, L.; Liang, S.; Wu, W.; Liang, R.; Wu, L. Multifunctional NH_2-mediated zirconium metal–organic framework as an efficient visible-light-driven photocatalyst for selective oxidation of alcohols and reduction of aqueous Cr(VI). *Dalton Trans.* **2013**, *42*, 13649–13657. [CrossRef] [PubMed]
9. Thommes, M.; Kaneko, K.; Neimark, A.V.; Olivier, J.P.; Rodriguez-Reinoso, F.; Rouquerol, J.; Sing, K.S.W. Physisorption of gases, with special reference to the evaluation of surface area and pore size distribution (IUPAC Technical Report). *Pure Appl. Chem.* **2015**, *87*, 1051–1069. [CrossRef]
10. Cao, S.; Ye, X.; Hu, H.; Jin, H.; Wang, Y.; Ye, J. Rational synthesis of $SrTiO_3$ nanodots anchored mesocrystalline anatase TiO_2 submicrospheres for photocatalytic reduction of CrVI. *Sep. Purif. Technol.* **2021**, *275*, 119096. [CrossRef]
11. Li, S.; You, C.; Rong, K.; Zhuang, C.; Chen, X.; Zhang, B. Chemically bonded $Mn_{0.5}Cd_{0.5}S$/BiOBr S-scheme photocatalyst with rich oxygen vacancies for improved photocatalytic decontamination performance. *Adv. Powder Mater.* **2024**, *3*, 100183. [CrossRef]
12. Liang, Q.; Ploychompoo, S.; Chen, J.; Zhou, T.; Luo, H. Simultaneous Cr(VI) reduction and bisphenol A degradation by a 3D Z-scheme Bi_2S_3-$BiVO_4$ graphene aerogel under visible light. *Chem. Eng. J.* **2020**, *384*, 123256. [CrossRef]
13. Zhang, L.L.; Liu, X.Y.; Wang, Y.L.; Li, Y.; Zhu, X.G.; Cao, R.H.; Zhang, H.J.; Dong, X.Y.; Qin, J.H. Host-guest engineering in a two-dimensional anionic porphyrinic metal-organic framework via cationic bodipy encapsulation for boosting photocatalytic H_2 evolution. *J. Colloid Interface Sci.* **2026**, *724*, 141035. [CrossRef] [PubMed]
14. Zhang, Q.X.; Zhang, Y.T.; He, Z.C.; Zhang, J.; Chen, W.; Song, Z.; Wang, T.; Huang, G.B. Engineering Zn-O-W interfacial electron bridge and vacancy-mediated modulation in WO_{3-x} quantum dot-decorated ZnCdS heterojunction enabling enhanced activity toward hydrogen peroxide photosynthesis. *J. Mater. Sci. Technol.* **2027**, *277*, 76–84. [CrossRef]
15. Li, S.; Huang, Y.; Chen, T.; He, Z.C.; Wang, T.; Wang, M.; Liu, G.; Huang, G.B.; Chen, W. S-scheme $Zn_2In_2S_5$/CdS nanosheet-on-nanosheet heterostructures with tight interfacial contacts promote efficient H_2O_2 photoproduction from pure water. *J. Mater. Chem. A* **2026**, *14*, 23221–23230. [CrossRef]
16. Islam, J.B.; Furukawa, M.; Tateishi, I.; Katsumata, H.; Kaneco, S. Photocatalytic reduction of hexavalent chromium with nanosized TiO_2 in presence of formic acid. *ChemEngineering* **2019**, *3*, 33. [CrossRef]
17. Nanda, B.; Pradhan, A.C.; Parida, K.M. Fabrication of mesoporous CuO/ZrO_2-MCM-41 nanocomposites for photocatalytic reduction of Cr(VI). *Chem. Eng. J.* **2017**, *316*, 1122–1135. [CrossRef]
18. Yan, R.; Luo, D.; Fu, C.; Tian, W.; Wu, P.; Wang, Y.; Zhang, H.; Jiang, W. Simultaneous Removal of Cu(II) and Cr(VI) Ions from Wastewater by Photoreduction with TiO_2–ZrO_2. *J. Water Process Eng.* **2020**, *33*, 101052. [CrossRef]
19. Alsheheri, S.Z.; Shawky, A.; Alsaggaf, W.T.; Zaki, Z.I. Visible-light responsive ZnSe-anchored mesoporous TiO_2 heterostructures for boosted photocatalytic reduction of Cr(VI). *Nanotechnology* **2022**, *33*, 305701. [CrossRef] [PubMed]

20. Skliri, E.; Vamvasakis, I.; Papadas, I.T.; Choulis, S.A.; Armatas, G.S. Mesoporous Composite Networks of Linked $MnFe_2O_4$ and $ZnFe_2O_4$ Nanoparticles as Efficient Photocatalysts for the Reduction of Cr(VI). *Catalysts* **2021**, *11*, 199. [CrossRef]
21. Zhao, F.; Liu, Y.; Hammouda, S.B.; Doshi, B.; Guijarro, N.; Min, X.; Tang, C.J.; Sillanpää, M.; Sivula, K.; Wang, S. MIL-101(Fe)/g-C_3N_4 for enhanced visible-light-driven photocatalysis toward simultaneous reduction of Cr(VI) and oxidation of bisphenol A in aqueous media. *Appl. Catal. B Environ.* **2020**, *272*, 119033. [CrossRef]
22. Huang, Y.; Zhao, M.; Li, G.; Lin, Y.; Wang, L. Far-UVC-driven Cr(VI) reduction in alkaline solution: Synergistic effects of iodide and sulfite. *J. Environ. Sci.* **2026**, *160*, 405–413. [CrossRef] [PubMed]
23. Loryuenyong, V.; Jarunsak, N.; Chuangchai, T.; Buasri, A. The Photocatalytic Reduction of Hexavalent Chromium by Controllable Mesoporous Anatase TiO_2 Nanoparticles. *Adv. Mater. Sci. Eng.* **2014**, *2014*, 348427. [CrossRef]
24. Jin, C.Z.; Yang, Y.; Yang, X.A.; Wang, S.B.; Zhang, W.B. Visible photocatalysis of Cr(VI) at g/L level in Si/N-TiO_2 nanocrystals synthesized by one-step co-hydrolysis method. *Chem. Eng. J.* **2020**, *398*, 125641. [CrossRef]
25. Zhai, X.M.; Yang, X.A.; Liu, X.N.; Dong, Y.P.; Zhang, W.B. Sensitive photocatalytic reduction of high concentration chromium-containing wastewater driven by one-step hydrothermal synthesis of bi-element modified TiO_2. *Appl. Surf. Sci.* **2023**, *622*, 156976. [CrossRef]
26. Wang, S.; Zhang, Z.; Huo, W.; Zhang, X.; Fang, F.; Xie, Z.; Jiang, J. Single-crystal-like black Zr-TiO_2 nanotube array film: An efficient photocatalyst for fast reduction of Cr(VI). *Chem. Eng. J.* **2021**, *403*, 126331. [CrossRef]
27. Yang, H.; Yang, Y.; Jiang, L.; Wang, Y.; Chen, Y.; He, J.; Wang, W.; Wang, J. Photocatalytic reduction of Cr(VI) within mesoporous TiO_2 templated and confined with chlorophyll. *Nano Sel.* **2022**, *3*, 140–146. [CrossRef]
28. Tu, B.; Chen, H.; Deng, J.; Xue, S.; Ma, X.; Xu, Y.; Xie, Z.; Tao, H. Preparation of N-I co-doped TiO_2 supported on activated carbon photocatalyst for efficient photocatalytic reduction of Cr(VI) ions. *Colloids Surf. A Physicochem. Eng. Asp.* **2021**, *622*, 126660. [CrossRef]
29. Shaikh, A.; Mishra, S.P.; Mohapatra, P.; Parida, S. One-step solvothermal synthesis of TiO_2-reduced graphene oxide nanocomposites with enhanced visible light photoreduction of Cr(VI). *J. Nanoparticle Res.* **2017**, *19*, 206. [CrossRef]
30. Djellabi, R.; Yang, B.; Wang, Y.; Cui, X.; Zhao, X. Carbonaceous biomass-titania composites with Ti O C bonding bridge for efficient photocatalytic reduction of Cr(VI) under narrow visible light. *Chem. Eng. J.* **2019**, *366*, 172–180. [CrossRef]
31. Shan, Y.; Cui, J.; Liu, Y.; Zhao, W. TiO_2 anchored on MoS_2 nanosheets based on molybdenite exfoliation as an efficient cathode for enhanced Cr(VI) reduction in microbial fuel cell. *Environ. Res.* **2020**, *190*, 110010. [CrossRef] [PubMed]
32. Wang, N.; Zhang, F.; Mei, Q.; Wu, R.; Wang, W. Photocatalytic TiO_2/rGO/CuO Composite for Wastewater Treatment of Cr(VI) Under Visible Light. *Water Air Soil Pollut.* **2020**, *231*, 223. [CrossRef]
33. Cao, D.; Guan, J.; Du, J.; Sun, Q.; Ma, J.; Li, J.; Liu, J.; Sheng, G. Halogen-functionalized covalent organic frameworks for photocatalytic Cr(VI) reduction under visible light. *J. Hazard. Mater.* **2024**, *476*, 134956. [CrossRef] [PubMed]
34. Wang, X.; Xu, J.; Liu, S.; Yang, W.; Chen, Y.; Zhang, Y. Synthesis of TiO_2/MOF-801(Zr) by a wet impregnation at room temperature for highly efficient photocatalytic reduction of Cr(VI). *Solid State Sci.* **2022**, *129*, 106912. [CrossRef]
35. Wang, X.; Liu, J.; Leong, S.; Lin, X.; Wei, J.; Kong, B.; Xu, Y.; Low, Z.X.; Yao, J.; Wang, H. Rapid Construction of ZnO@ZIF-8 Heterostructures with Size-Selective Photocatalysis Properties. *ACS Appl. Mater. Interfaces* **2016**, *8*, 9080–9087. [CrossRef] [PubMed]
36. Tu, H.; Wang, H.; Zhang, J.; Ou, Y.; Zhang, Z.; Chen, G.; Wei, C.; Xiang, X.; Xie, Z. A novel hierarchical 0D/3D NH_2-MIL-101(Fe)/$ZnIn_2S_4$ S-scheme heterojunction photocatalyst for efficient Cr(VI) reduction and photo-Fenton-like removal of 2-nitrophenol. *J. Environ. Chem. Eng.* **2024**, *12*, 111695. [CrossRef]
37. Ma, J.; Fan, L.; Wang, X.; Li, L.; Zhang, Y.; Zhao, G.; Chai, B.; Gao, J. Defect engineering on metal-organic frameworks for enhanced photocatalytic reduction of Cr(VI). *Surf. Interfaces* **2024**, *54*, 105174. [CrossRef]
38. Wu, L.; Qin, D.; Fang, F.; Wang, W.; Zhao, W. Development of Efficient Photocatalyst MIL-68(Ga)_NH_2 Metal-Organic Framework for the Removal of Cr(VI) and Cr(VI)/RhB from Wastewater under Visible Light. *Materials* **2022**, *15*, 3761. [CrossRef] [PubMed]
39. Liang, R.; Huang, R.; Wang, X.; Ying, S.; Yan, G.; Wu, L. Functionalized MIL-68(In) for the photocatalytic treatment of Cr(VI)-containing simulation wastewater: Electronic effects of ligand substitution. *Appl. Surf. Sci.* **2019**, *464*, 396–403. [CrossRef]
40. Zhao, X.; Wu, L.; Chen, X.; Hu, J.; Wu, T.h.; Li, Q.; Lv, K. Excellent photoreduction performance of Cr(VI) over $(WO_4)^{2-}$ -doped metal organic framework materials. *New J. Chem.* **2020**, *44*, 20704–20714. [CrossRef]
41. Wang, L.; Chakraborty, J.; Rawat, K.S.; Deng, M.; Sun, J.; Wang, Y.; Speybroeck, V.V.; Van Der Voort, P. Totally conjugated and coplanar covalent organic frameworks as photocatalysts for water purification: Reduction of Cr(VI) while oxidizing water borne organic pollutants. *Sep. Purif. Technol.* **2025**, *359*, 130368. [CrossRef]
42. Chen, H.; Qi, C.; Zhang, S.; Zhou, Y. Engineering redox metal covalent organic frameworks for efficient chromium(VI) photoreduction. *Colloids Surf. A Physicochem. Eng. Asp.* **2025**, *719*, 136988. [CrossRef]
43. Yue, J.Y.; Wang, Y.T.; Ding, X.L.; Fan, Y.F.; Song, L.P.; Yang, P.; Ma, Y.; Tang, B. Single-atom substitution in donor–acceptor covalent organic frameworks for tunable visible light photocatalytic Cr(VI) reduction. *Mater. Chem. Front.* **2022**, *6*, 3748–3754. [CrossRef]

44. Qiu, J.; Zhang, X.; Xie, K.; Zhang, X.F.; Feng, Y.; Jia, M.; Yao, J. Noble metal nanoparticle-functionalized Zr-metal organic frameworks with excellent photocatalytic performance. *J. Colloid Interface Sci.* **2019**, *538*, 569–577. [CrossRef]
45. Wang, Q.; Li, H.; Yu, X.; Jia, Y.; Chang, Y.; Gao, S. Morphology regulated Bi_2WO_6 nanoparticles on TiO_2 nanotubes by solvothermal Sb^{3+} doping as effective photocatalysts for wastewater treatment. *Electrochim. Acta* **2020**, *330*, 135167. [CrossRef]
46. Xue, C.; Zhang, T.; Ding, S.; Wei, J.; Yang, G. Anchoring Tailored Low-Index Faceted BiOBr Nanoplates onto TiO_2 Nanorods to Enhance the Stability and Visible-Light-Driven Catalytic Activity. *ACS Appl. Mater. Interfaces* **2017**, *9*, 16091–16102. [CrossRef] [PubMed]
47. Zhang, X.; Li, X.; Shao, C.; Li, J.; Zhang, M.; Zhang, P.; Wang, K.; Lu, N.; Liu, Y. One-dimensional hierarchical heterostructures of In_2S_3 nanosheets on electrospun TiO_2 nanofibers with enhanced visible photocatalytic activity. *J. Hazard. Mater.* **2013**, *260*, 892–900. [CrossRef]
48. Wang, J.; Li, X.; Li, X.; Zhu, J.; Li, H. Mesoporous yolk–shell SnS_2–TiO_2 visible photocatalysts with enhanced activity and durability in Cr(VI) reduction. *Nanoscale* **2013**, *5*, 1876. [CrossRef] [PubMed]
49. Thankam Thomas, R.; Sandhyarani, N. Template free synthesis of graphitic carbon nitride/titania mesoflowers. *RSC Adv.* **2015**, *5*, 72683–72690. [CrossRef]
50. Zong, H.; Zhao, T.; Zhou, G.; Qian, R.; Feng, T.; Pan, J.H. Revisiting structural and photocatalytic properties of g-C_3N_4/TiO_2: Is surface modification of TiO_2 by calcination with urea an effective route to "solar" photocatalyst? *Catal. Today* **2019**, *335*, 252–261. [CrossRef]
51. Khazaee, Z.; Mahjoub, A.R.; Cheshme Khavar, A.H.; Srivastava, V.; Sillanpää, M. Sub-level engineering strategy of nitrogen-induced Bi_2O_3/g-C_3N_4: A versatile photocatalyst for oxidation and reduction. *Environ. Sci. Pollut. Res.* **2021**, *28*, 50747–50766. [CrossRef] [PubMed]
52. Zhang, X.; Yang, P.; Jiang, S.P. NiCo-layered double hydroxide/g-C_3N_4 heterostructures with enhanced adsorption capacity and photoreduction of Cr(VI). *Appl. Surf. Sci.* **2021**, *556*, 149772. [CrossRef]
53. Patnaik, S.; Das, K.K.; Mohanty, A.; Parida, K. Enhanced photo catalytic reduction of Cr(VI) over polymer-sensitized g-C_3N_4/$ZnFe_2O_4$ and its synergism with phenol oxidation under visible light irradiation. *Catal. Today* **2018**, *315*, 52–66. [CrossRef]
54. Wu, M.H.; Li, L.; Xue, Y.C.; Xu, G.; Tang, L.; Liu, N.; Huang, W.Y. Fabrication of ternary GO/g-C_3N_4/MoS_2 flower-like heterojunctions with enhanced photocatalytic activity for water remediation. *Appl. Catal. B Environ.* **2018**, *228*, 103–112. [CrossRef]
55. Yu, T.; Lv, L.; Wang, H.; Tan, X. Enhanced photocatalytic treatment of Cr(VI) and phenol by monoclinic $BiVO_4$ with {010}-orientation growth. *Mater. Res. Bull.* **2018**, *107*, 248–254. [CrossRef]
56. Jia, J.; Zhang, M.; Liu, Z.; Yu, C.; Zhou, W.; Li, Z. La^{3+},Gd^{3+}-codoped $BiVO_4$ nanorods with superior visible-light-driven photocatalytic performance for simultaneous removing aqueous Cr(VI) and azo dye. *J. Nanoparticle Res.* **2020**, *22*, 275. [CrossRef]
57. Liu, X.; Ren, A.; Liu, A.; Jiang, X.; Zhang, L. Simultaneous photocatalytic tetracycline oxidation and Cr(VI) reduction by a 0D/3D hierarchical Bi_2WO_6@CoO Z-scheme heterostructure: In situ interfacial engineering and charge regulation mechanism. *J. Environ. Manag.* **2023**, *342*, 118134. [CrossRef] [PubMed]
58. Zhao, W.; Li, J.; Dai, B.; Cheng, Z.; Xu, J.; Ma, K.; Zhang, L.; Sheng, N.; Mao, G.; Wu, H.; et al. Simultaneous removal of tetracycline and Cr(VI) by a novel three-dimensional AgI/$BiVO_4$ p-n junction photocatalyst and insight into the photocatalytic mechanism. *Chem. Eng. J.* **2019**, *369*, 716–725. [CrossRef]
59. Sang, Y.; Xue, J.; Hu, J.; Zhang, P.; Zhao, F.; He, Y. Enhanced photocatalytic reduction of Cr(VI) using porous hierarchical Bi_2O_3/Bi_2S_3 high-low heterojunctions: Novel strategies and charge transfer mechanisms. *Colloids Surf. A Physicochem. Eng. Asp.* **2024**, *700*, 134808. [CrossRef]
60. Vavilapalli, D.S.; Qin, L.; Shamshirgar, A.S.; Rosen, J. Efficient photocatalytic reduction of aqueous Cr(VI) by MXene-(Ti_3C_2, $Mo_{4/3}C$) and $Ca_2Fe_2O_5$-based nanocomposites. *J. Environ. Chem. Eng.* **2025**, *13*, 116169. [CrossRef]
61. Zhang, Y.; Luo, J.; Wang, X.; Zhang, D.; Xu, H.; Sun, Y.; Gu, X.; Hu, X.; Gao, B.; Ren, H. Photoresponse of $Ti_3C_2T_x$ MXene promotes its adsorptive-reductive removal of Cr(VI) from water. *J. Environ. Manag.* **2024**, *370*, 122673. [CrossRef] [PubMed]
62. Yin, H.; Pu, B.; Jiang, H.; He, H.; Han, T.; Wang, W.; Yu, C.; Wang, Z.; Li, X. Highly Active MXene Quantum Dots/CuSe n-p Plasmonic Heterostructures for Ultrafast Photocatalytic Removal of Cr(VI) under Full Solar Spectrum. *Langmuir* **2024**, *40*, 24484–24493. [CrossRef] [PubMed]
63. Ghoreishian, S.M.; Ranjith, K.S.; Park, B.; Hwang, S.-K.; Hosseini, R.; Behjatmanesh-Ardakani, R.; Pourmortazavi, S.M.; Lee, H.U.; Son, B.; Mirsadeghi, S.; et al. Full-spectrum-responsive Bi_2S_3@CdS S-scheme heterostructure with intimated ultrathin RGO toward photocatalytic Cr(VI) reduction and H_2O_2 production: Experimental and DFT studies. *Chem. Eng. J.* **2021**, *419*, 129530. [CrossRef]
64. Ren, J.; Hu, T.; Gong, Q.; Wang, Q.; Sun, B.; Gao, T.; Cao, P.; Zhou, G. Spherical bi2 Wo6/Bi_2S_3/MoS_2 n-p heterojunction with excellent visible-light photocatalytic reduction Cr(VI) activity. *Nanomaterials* **2020**, *10*, 1813. [CrossRef] [PubMed]
65. Patnaik, S.; Sahoo, D.P.; Parida, K.M. Bimetallic co-effect of Au-Pd alloyed nanoparticles on mesoporous silica modified g-C_3N_4 for single and simultaneous photocatalytic oxidation of phenol and reduction of hexavalent chromium. *J. Colloid Interface Sci.* **2020**, *560*, 519–535. [CrossRef] [PubMed]

66. Koutsouroubi, E.D.; Vamvasakis, I.; Minotaki, M.G.; Papadas, I.T.; Drivas, C.; Choulis, S.A.; Kopidakis, G.; Kennou, S.; Armatas, G.S. Ni-doped MoS_2 modified graphitic carbon nitride layered hetero-nanostructures as highly efficient photocatalysts for environmental remediation. *Appl. Catal. B Environ.* **2021**, *297*, 120419. [CrossRef]
67. Chachvalvutikul, A.; Luangwanta, T.; Kaowphong, S. Double Z-scheme $FeVO_4/Bi_4O_5Br_2$/BiOBr ternary heterojunction photocatalyst for simultaneous photocatalytic removal of hexavalent chromium and rhodamine B. *J. Colloid Interface Sci.* **2021**, *603*, 738–757. [CrossRef] [PubMed]
68. Tu, H.; Wang, H.; Ou, Y.; Zhang, J.; Jiang, S.; Xiong, Y.; Xiang, X.; Wei, C.; Liu, X. A novel MOF-derived CoSx@$ZnIn_2S_4/MoS_2$ QDs dual Z-scheme heterojunction photocatalyst with hierarchical hollow core-shell structure for enhanced photocatalytic performance. *J. Environ. Chem. Eng.* **2025**, *13*, 118981. [CrossRef]
69. Aziz, F.F.A.; Jalil, A.A.; Hassan, N.S.; Fauzi, A.A.; Azami, M.S. Simultaneous photocatalytic reduction of hexavalent chromium and oxidation of p-cresol over AgO decorated on fibrous silica zirconia. *Environ. Pollut.* **2021**, *285*, 117490. [CrossRef] [PubMed]
70. Wang, Y.; Li, W.; Duan, W.; Cui, R.; Liao, G.; Wang, N. Hydrophilicity improvement of PVDF-networked CdS/TiO_2 photocatalytic membrane for flat-panel purification of pharmaceutical wastewater accompanied by Cr(VI) reduction. *Chem. Eng. J.* **2025**, *519*, 165220. [CrossRef]
71. Bortot Coelho, F.E.; Candelario, V.M.; Araújo, E.M.R.; Miranda, T.L.S.; Magnacca, G. Photocatalytic Reduction of Cr(VI) in the Presence of Humic Acid Using Immobilized Ce–ZrO_2 under Visible Light. *Nanomaterials* **2020**, *10*, 779. [CrossRef] [PubMed]
72. Eskandarloo, H.; Badiei, A.; Behnajady, M.A.; Ziarani, G.M. Minimization of electrical energy consumption in the photocatalytic reduction of Cr(VI) by using immobilized Mg, Ag co-impregnated TiO_2 nanoparticles. *RSC Adv.* **2014**, *4*, 28587. [CrossRef]
73. Bai, J.; Wang, C.; Zhang, X.; Li, X.; Mao, Y.; Liang, W.; Zhang, C.; Xiao, X.; Shen, J. Revealing multi-level shortrange migration of electrons on full-spectrum response e-LDH/t-BiOCl/Bi_2S_3 and their essential role in the detoxification of Cr(VI) and refractory organic pollutants. *Environ. Res.* **2025**, *266*, 120479. [CrossRef] [PubMed]
74. Zhang, Y.; Zhao, Y.; Xu, Z.; Su, H.; Bian, X.; Zhang, S.; Dong, X.; Zeng, L.; Zeng, T.; Feng, M.; et al. Carbon quantum dots implanted CdS nanosheets: Efficient visible-light-driven photocatalytic reduction of Cr(VI) under saline conditions. *Appl. Catal. B Environ.* **2020**, *262*, 118306. [CrossRef]
75. Liu, Y.; Du, X.; Huang, Z. Photocatalytic reduction of aqueous chromium(VI) by RuO_2/g-C_3N_4 composite under visible light irradiation. *RSC Adv.* **2025**, *15*, 16724–16733. [CrossRef] [PubMed]
76. Gowland, D.C.A.; Robertson, N.; Chatzisymeon, E. Life cycle assessment of immobilised and slurry photocatalytic systems for removal of natural organic matter in water. *Environments* **2024**, *11*, 114. [CrossRef]
77. Du, Y.; Tao, Z.; Guan, J.; Sun, Z.; Zeng, W.; Wen, P.; Ni, K.; Ye, J.; Yang, S.; Du, P.; et al. Microwave-assisted synthesis of hematite/activated graphene composites with superior performance for photocatalytic reduction of Cr(VI). *RSC Adv.* **2015**, *5*, 81438–81444. [CrossRef]
78. Sanad, M.M.S.; Abdel-Aal, E.A.; Osman, H.M.; Kandil, A.T. Photocatalytic reduction of hexavalent chromium with commercial Fe/Ti oxide catalyst under UV and visible light irradiation. *Int. J. Environ. Sci. Technol.* **2018**, *15*, 2459–2472. [CrossRef]
79. Boonprakob, N.; Channei, D.; Zhao, C. Heterogeneous photocatalytic reduction of hexavalent chromium by modified Ag, Cu co-doped tungsten oxide nanoparticles. *J. Aust. Ceram. Soc.* **2021**, *57*, 743–754. [CrossRef]
80. Ibrahim, I.; Kaltzoglou, A.; Athanasekou, C.; Katsaros, F.; Devlin, E.; Kontos, A.G.; Ioannidis, N.; Perraki, M.; Tsakiridis, P.; Sygellou, L.; et al. Magnetically separable $TiO_2/CoFe_2O_4$/Ag nanocomposites for the photocatalytic reduction of hexavalent chromium pollutant under UV and artificial solar light. *Chem. Eng. J.* **2020**, *381*, 122730. [CrossRef]
81. Velegraki, G.; Vamvasakis, I.; Papadas, I.T.; Tsatsos, S.; Pournara, A.; Manos, M.J.; Choulis, S.A.; Kennou, S.; Kopidakis, G.; Armatas, G.S. Boosting photochemical activity by Ni doping of mesoporous CoO nanoparticle assemblies. *Inorg. Chem. Front.* **2019**, *6*, 765–774. [CrossRef]
82. Zheng, J.; Lei, Z. Incorporation of CoO nanoparticles in 3D marigold flower-like hierarchical architecture $MnCo_2O_4$ for highly boosting solar light photo-oxidation and reduction ability. *Appl. Catal. B Environ.* **2018**, *237*, 1–8. [CrossRef]
83. Lu, Y.; Song, J.; Li, W.; Pan, Y.; Fang, H.; Wang, X.; Hu, G. Preparation of BiOCl/Bi_2S_3 composites by simple ion exchange method for highly efficient photocatalytic reduction of Cr^{6+}. *Appl. Surf. Sci.* **2020**, *506*, 145000. [CrossRef]
84. Skliri, E.; Miao, J.; Xie, J.; Liu, G.; Salim, T.; Liu, B.; Zhang, Q.; Armatas, G.S. Assembly and photochemical properties of mesoporous networks of spinel ferrite nanoparticles for environmental photocatalytic remediation. *Appl. Catal. B Environ.* **2018**, *227*, 330–339. [CrossRef]
85. Zhang, G.; Chen, D.; Li, N.; Xu, Q.; Li, H.; He, J.; Lu, J. Fabrication of Bi_2MoO_6/ZnO hierarchical heterostructures with enhanced visible-light photocatalytic activity. *Appl. Catal. B Environ.* **2019**, *250*, 313–324. [CrossRef]
86. Zhao, W.; Dong, Q.; Sun, C.; Xia, D.; Huang, H.; Yang, G.; Wang, G.; Leung, D.Y.C. A novel Au/g-C_3N_4 nanosheets/CeO_2 hollow nanospheres plasmonic heterojunction photocatalysts for the photocatalytic reduction of hexavalentchromium and oxidation of oxytetracycline hydrochloride. *Chem. Eng. J.* **2021**, *409*, 128185. [CrossRef]
87. Liang, J.; Jing, C.; Wang, J.; Men, Y. Photocatalytic Reduction of Cr(VI) over g-C_3N_4 Photocatalysts Synthesized by Different Precursors. *Molecules* **2021**, *26*, 7054. [CrossRef] [PubMed]

88. Hasija, V.; Raizada, P.; Singh, P.; Verma, N.; Khan, A.A.P.; Singh, A.; Selvasembian, R.; Kim, S.Y.; Hussain, C.M.; Nguyen, V.H.; et al. Progress on the photocatalytic reduction of hexavalent Cr(VI) using engineered graphitic carbon nitride. *Process Saf. Environ. Prot.* **2021**, *152*, 663–678. [CrossRef]
89. Li, M.; Hu, Q.; Shan, H.; Yu, W.; Xu, Z.X. Fabrication of copper phthalocyanine/reduced graphene oxide nanocomposites for efficient photocatalytic reduction of hexavalent chromium. *Chemosphere* **2021**, *263*, 128250. [CrossRef] [PubMed]
90. Padhi, D.K.; Pradhan, G.K.; Parida, K.M.; Singh, S.K. Facile fabrication of $Gd(OH)_3$ nanorod/RGO composite: Synthesis, characterisation and photocatalytic reduction of Cr(VI). *Chem. Eng. J.* **2014**, *255*, 78–88. [CrossRef]
91. Koutsouroubi, E.D.; Vamvasakis, I.; Drivas, C.; Kennou, S.; Armatas, G.S. Photochemical deposition of SnS_2 on graphitic carbon nitride for photocatalytic aqueous Cr(VI) reduction. *Chem. Eng. J. Adv.* **2022**, *9*, 100224. [CrossRef]
92. Wang, Y.; Wu, L.; Hu, Y.; Du, H.; Liu, P.; Hao, L.; Guan, H.; Zhao, Y. Constructing flower-like $MoS_2/ZnIn_2S_4$ microspheres for efficient visible light-driven photocatalytic removal of hexavalent chromium. *J. Mater. Sci. Mater. Electron.* **2022**, *33*, 16113–16125. [CrossRef]
93. Djellabi, R.; Yang, B.; Xiao, K.; Gong, Y.; Cao, D.; Sharif, H.M.A.; Zhao, X.; Zhu, C.; Zhang, J. Unravelling the mechanistic role of Ti O C bonding bridge at titania/lignocellulosic biomass interface for Cr(VI) photoreduction under visible light. *J. Colloid Interface Sci.* **2019**, *553*, 409–417. [CrossRef] [PubMed]
94. Yanagida, S.; Yajima, T.; Takei, T.; Kumada, N. Removal of hexavalent chromium from water by Z-scheme photocatalysis using TiO_2 (rutile) nanorods loaded with Au core–Cu_2O shell particles. *J. Environ. Sci.* **2022**, *115*, 173–189. [CrossRef] [PubMed]
95. Chen, Z.; Li, Y.; Guo, M.; Xu, F.; Wang, P.; Du, Y.; Na, P. One-pot synthesis of Mn-doped TiO 2 grown on graphene and the mechanism for removal of Cr(VI) and Cr(III). *J. Hazard. Mater.* **2016**, *310*, 188–198. [CrossRef] [PubMed]
96. Faisal, M.; Harraz, F.A.; Al-Salami, A.E.; El-Toni, A.M.; Almadiy, A.A.; Khan, A.; Labis, J.P.; Al-Sayari, S.A.; Al-Assiri, M.S. Enhanced photocatalytic reduction of Cr(VI) on silver nanoparticles modified mesoporous silicon under visible light. *J. Am. Ceram. Soc.* **2019**, *102*, 5071–5081. [CrossRef]
97. Kohantorabi, M.; Moussavi, G.; Oulego, P.; Giannakis, S. Synthesis of a novel, ternary AgI/CeO_2@g-C_3N_4 nanocomposite with exceptional stability and reusability for visible light-assisted photocatalytic reduction of hexavalent chromium. *Appl. Surf. Sci.* **2021**, *555*, 149692. [CrossRef]
98. Xia, Q.; Huang, B.; Yuan, X.; Wang, H.; Wu, Z.; Jiang, L.; Xiong, T.; Zhang, J.; Zeng, G.; Wang, H. Modified stannous sulfide nanoparticles with metal-organic framework: Toward efficient and enhanced photocatalytic reduction of chromium (VI) under visible light. *J. Colloid Interface Sci.* **2018**, *530*, 481–492. [CrossRef] [PubMed]
99. Song, Y.; Lu, X.; Liu, Z.; Liu, W.; Gai, L.; Gao, X.; Ma, H. Efficient Removal of Cr(VI) by TiO_2 Based Micro-Nano Reactor via the Synergy of Adsorption and Photocatalysis. *Nanomaterials* **2022**, *12*, 291. [CrossRef] [PubMed]
100. Liu, Q.; Zhou, B.; Xu, M.; Mao, G. Integration of nanosized ZIF-8 particles onto mesoporous TiO_2 nanobeads for enhanced photocatalytic activity. *RSC Adv.* **2017**, *7*, 8004–8010. [CrossRef]
101. Choi, D.; Ham, S.; Jang, D.J. Visible-light photocatalytic reduction of Cr(VI) via carbon quantum dots-decorated TiO_2 nanocomposites. *J. Environ. Chem. Eng.* **2018**, *6*, 1–8. [CrossRef]
102. Bayrak, R.; Albay, C.; Koç, M.; Altın, İ.; Değirmencioğlu, İ.; Sökmen, M. Preparation of phthalocyanine/TiO_2 nanocomposites for photocatalytic removal of toxic Cr(VI) ions. *Process Saf. Environ. Prot.* **2016**, *102*, 294–302. [CrossRef]
103. Chen, F.; Yu, W.; Qie, Y.; Zhao, L.; Zhang, H.; Guo, L.-H. Enhanced photocatalytic removal of hexavalent chromium through localized electrons in polydopamine-modified TiO_2 under visible irradiation. *Chem. Eng. J.* **2019**, *373*, 58–67. [CrossRef]
104. Mirghani, M. Synthesis and characterizations of molybdenum-doped titanium dioxide nanoparticles for photocatalytic removal of chromium (VI) from aqueous solutions. *Nanocomposites* **2024**, *10*, 59–67. [CrossRef]
105. Zhang, Y.C.; Yang, M.; Zhang, G.; Dionysiou, D.D. HNO_3-involved one-step low temperature solvothermal synthesis of N-doped TiO_2 nanocrystals for efficient photocatalytic reduction of Cr(VI) in water. *Appl. Catal. B Environ.* **2013**, *142–143*, 249–258. [CrossRef]
106. Sun, Y.; Xu, L.; Jin, P.; Bai, X.; Jin, X.; Shi, X. Simultaneous removal of colorless micropollutants and hexavalent chromium by pristine TiO_2 under visible light: An electron transfer mechanism. *Chem. Eng. J.* **2021**, *405*, 126968. [CrossRef]
107. Yang, J.; Dai, J.; Li, J. Visible-light-induced photocatalytic reduction of Cr(VI) with coupled Bi_2O_3/TiO_2 photocatalyst and the synergistic bisphenol A oxidation. *Environ. Sci. Pollut. Res.* **2013**, *20*, 2435–2447. [CrossRef] [PubMed]
108. Xu, J.; Xu, Z.; Zhang, M.; Xu, J.; Fang, D.; Ran, W. Impregnation synthesis of TiO_2/hydroniumjarosite composite with enhanced property in photocatalytic reduction of Cr(VI). *Mater. Chem. Phys.* **2015**, *152*, 4–8. [CrossRef]
109. Ding, Y.; Maitra, S.; Wang, C.; Zheng, R.; Barakat, T.; Roy, S.; Chen, L.H.; Su, B.L. Bi-functional Cu-TiO_2/CuO photocatalyst for large-scale synergistic treatment of waste sewage containing organics and heavy metal ions. *Sci. China Mater.* **2023**, *66*, 179–192. [CrossRef]
110. Chen, C.-R.; Zeng, H.-Y.; Xu, S.; Shen, J.-C.; Hu, G.; Zhu, R.-L.; Du, J.-Z.; Sun, Y.-X. Facile fabrication of CdS/ZnAlO heterojunction with enhanced photocatalytic activity for Cr(VI) reduction under visible light. *Appl. Clay Sci.* **2018**, *165*, 197–204. [CrossRef]

111. Yang, Y.; Yan, L.; Li, J.; Li, J.; Yan, T.; Sun, M.; Pei, Z. Synergistic adsorption and photocatalytic reduction of Cr(VI) using Zn-Al-layered double hydroxide and TiO_2 composites. *Appl. Surf. Sci.* **2019**, *492*, 487–496. [CrossRef]
112. Kebir, M.; Trari, M.; Maachi, R.; Nasrallah, N.; Bellal, B.; Amrane, A. Relevance of a hybrid process coupling adsorption and visible light photocatalysis involving a new hetero-system $CuCo_2O_4/TiO_2$ for the removal of hexavalent chromium. *J. Environ. Chem. Eng.* **2015**, *3*, 548–559. [CrossRef]
113. Kaur, M.; Singh, J.; Chauhan, M.; Kumar, V.; Singh, K. Green synthesis of TiO_2-Al_2O_3-$ZnFe_2O_4$ nanocomposite using the Hibiscus rosa sinesis and evaluation of its photocatalytic applications. *Open Ceram.* **2024**, *18*, 100571. [CrossRef]
114. Das, K.K.; Patnaik, S.; Nanda, B.; Pradhan, A.C.; Parida, K. $ZnFe_2O_4$-Decorated Mesoporous Al_2O_3 Modified MCM-41: A Solar-Light-Active Photocatalyst for the Effective Removal of Phenol and Cr(VI) from Water. *ChemistrySelect* **2019**, *4*, 1806–1819. [CrossRef]
115. Liu, H.Y.; Niu, C.G.; Guo, H.; Liang, C.; Huang, D.W.; Zhang, L.; Yang, Y.Y.; Li, L. In suit constructing 2D/1D $MgIn_2S_4$/CdS heterojunction system with enhanced photocatalytic activity towards treatment of wastewater and H_2 production. *J. Colloid Interface Sci.* **2020**, *576*, 264–279. [CrossRef] [PubMed]
116. Zhao, M.; Wang, W.; Huang, C.; Dong, W.; Wang, Y.; Cheng, S.; Wang, H.; Qian, H. Facile synthesis of UCNPs/$Zn_xCd_{1-x}S$ nanocomposites excited by near-infrared light for photochemical reduction and removal of Cr(VI). *Chin. J. Catal.* **2018**, *39*, 1240–1248. [CrossRef]
117. Qiang, T.; Chen, L.; Xia, Y.; Qin, X. Dual modified MoS_2/SnS_2 photocatalyst with Z-scheme heterojunction and vacancies defects to achieve a superior performance in Cr(VI) reduction and dyes degradation. *J. Clean. Prod.* **2021**, *291*, 125213. [CrossRef]
118. Fu, S.; Yuan, W.; Liu, X.; Yan, Y.; Liu, H.; Li, L.; Zhao, F.; Zhou, J. A novel 0D/2D WS_2/BiOBr heterostructure with rich oxygen vacancies for enhanced broad-spectrum photocatalytic performance. *J. Colloid Interface Sci.* **2020**, *569*, 150–163. [CrossRef] [PubMed]
119. Ma, H.; Liu, J.; Wang, Y.; Zuo, S.; Yu, Y.; Li, B. Construction of novel flower-like functionalized black phosphorus nanosheets/P-doped BiOCl S-scheme photocatalysts with improved photocatalytic activity in RhB and Cr(VI) degradation. *Mater. Adv.* **2022**, *3*, 7546–7558. [CrossRef]
120. Hu, X.; Zhang, G.; Yin, C.; Li, C.; Zheng, S. Facile fabrication of heterogeneous TiO_2/BiOCl composite with superior visible-light-driven performance towards Cr(VI) and tetracycline. *Mater. Res. Bull.* **2019**, *119*, 110559. [CrossRef]
121. Sedaghati, N.; Habibi-Yangjeh, A.; Asadzadeh-Khaneghah, S.; Ghosh, S. Photocatalytic performance of oxygen vacancy rich-TiO_2 combined with $Bi_4O_5Br_2$ nanoparticles on degradation of several water pollutants. *Adv. Powder Technol.* **2021**, *32*, 304–316. [CrossRef]
122. Zhang, G.; Sun, J.; Chen, D.; Li, N.; Xu, Q.; Li, H.; He, J.; Lu, J. Hierarchical core–shell heterostructures of $ZnIn_2S_4$ nanosheets on electrospun In_2O_3 nanofibers with highly enhanced photocatalytic activity. *J. Hazard. Mater.* **2020**, *398*, 122889. [CrossRef] [PubMed]
123. Deng, L.; Liu, H.; Gao, X.; Su, X.; Zhu, Z. SnS_2/TiO_2 nanocomposites with enhanced visible light-driven photoreduction of aqueous Cr(VI). *Ceram. Int.* **2016**, *42*, 3808–3815. [CrossRef]
124. Bao, J.; Jiang, X.; Huang, L.; Quan, W.; Zhang, C.; Wang, Y.; Wang, H.; Zeng, Y.; Zhang, W.; Ma, Y.; et al. Molybdenum disulfide loading on a Z-scheme graphitic carbon nitride and lanthanum nickelate heterojunction for enhanced photocatalysis: Interfacial charge transfer and mechanistic insights. *J. Colloid Interface Sci.* **2022**, *611*, 684–694. [CrossRef] [PubMed]
125. Liu, Y.; Ma, Y.J.; Liu, C.Y.; Zhang, Z.Y.; Yang, W.D.; Nie, S.D.; Zhou, X.H. The effective removal of Cr(VI) ions by carbon dot–silica hybrids driven by visible light. *RSC Adv.* **2016**, *6*, 68530–68537. [CrossRef]
126. Karthik, P.; Vinoth, R.; Selvam, P.; Balaraman, E.; Navaneethan, M.; Hayakawa, Y.; Neppolian, B. A visible-light active catechol–metal oxide carbonaceous polymeric material for enhanced photocatalytic activity. *J. Mater. Chem. A* **2017**, *5*, 384–396. [CrossRef]
127. Raza, W.; Faraz, M. Novel g-C_3N_4/Fe-ZnO/RGO nanocomposites with boosting visible light photocatalytic activity for MB, Cr(VI), and outstanding catalytic activity toward para-nitrophenol reduction. *Nanotechnology* **2020**, *31*, 325603. [CrossRef] [PubMed]
128. Zhang, F.; Wen, Q.; Hong, M.; Zhuang, Z.; Yu, Y. Efficient and sustainable metal-free GR/C_3N_4/CDots ternary heterostructrues for versatile visible-light-driven photoredox applications: Toward synergistic interaction of carbon materials. *Chem. Eng. J.* **2017**, *307*, 593–603. [CrossRef]
129. Hussain, M.B.; Azhar, U.; Loussala, H.M.; Razaq, R. Synergetic effect of $ZnIn_2S_4$ nanosheets with metal-organic framework molding heterostructure for efficient visible- light driven photocatalytic reduction of Cr(VI). *Arab. J. Chem.* **2020**, *13*, 5939–5948. [CrossRef]
130. Jing, F.; Liang, R.; Xiong, J.; Chen, R.; Zhang, S.; Li, Y.; Wu, L. MIL-68(Fe) as an efficient visible-light-driven photocatalyst for the treatment of a simulated waste-water contain Cr(VI) and Malachite Green. *Appl. Catal. B Environ.* **2017**, *206*, 9–15. [CrossRef]
131. Shi, H.; Yu, Y.; Zhang, Y.; Feng, X.; Zhao, X.; Tan, H.; Khan, S.U.; Li, Y.; Wang, E. Polyoxometalate/TiO_2/Ag composite nanofibers with enhanced photocatalytic performance under visible light. *Appl. Catal. B Environ.* **2018**, *221*, 280–289. [CrossRef]
132. Yu, Y.; Lu, Z.; Wei, H.; Cao, X.; Li, K. Electrostatic Self-assembly Aided Synthesis of CdS/$Cs_3PW_{12}O_{40}$ Hybrids for Photocatalytic Reduction of Cr(VI). *Water Air Soil Pollut.* **2020**, *231*, 345. [CrossRef]

133. Zou, X.; Shi, R.; Zhang, Z.; Fu, G.; Li, L.; Yu, L.; Tian, Y.; Luo, F. Calcined ZnTi-Layered Double Hydroxide Intercalated with $H_3PW_{12}O_{40}$ with Efficiently Photocatalytic and Adsorption Performances. *Chem.—Eur. J.* **2021**, *27*, 16670–16681. [CrossRef] [PubMed]
134. Na, D.; Jiang, L.; Li, M.; Lei, T.; Liu, Q.; He, J.; Chen, Y.; Wang, W.; Wang, J. One-pot synthesis of $Bi_3O(PO_4)_2(OH)$ embedded on rod-like $BiPO_4$ for efficient adsorption and visible-light photocatalytic reduction of aqueous Cr(VI). *J. Alloys Compd.* **2021**, *881*, 160518. [CrossRef]
135. Li, X.; Chen, D.; Li, N.; Xu, Q.; Li, H.; He, J.; Lu, J. Efficient reduction of Cr(VI) by a BMO/Bi_2S_3 heterojunction via synergistic adsorption and photocatalysis under visible light. *J. Hazard. Mater.* **2020**, *400*, 123243. [CrossRef] [PubMed]
136. Fu, B.; Sun, H.; Liu, J.; Zhou, T.; Chen, M.; Cai, Z.; Hao, D.; Zhu, X. Construction of MIL-125-NH_2@$BiVO_4$ Composites for Efficient Photocatalytic Dye Degradation. *ACS Omega* **2022**, *7*, 26201–26210. [CrossRef] [PubMed]
137. Jia, J.; Xue, P.; Wang, R.; Bai, X.; Hu, X.; Fan, J.; Liu, E. The Bi/Bi_2WO_6 heterojunction with stable interface contact and enhanced visible-light photocatalytic activity for phenol and Cr(VI) removal. *J. Chem. Technol. Biotechnol.* **2018**, *93*, 2988–2999. [CrossRef]
138. Cai, J.; Wu, X.; Li, S.; Zheng, F. Controllable location of Au nanoparticles as cocatalyst onto TiO_2@CeO_2 nanocomposite hollow spheres for enhancing photocatalytic activity. *Appl. Catal. B Environ.* **2017**, *201*, 12–21. [CrossRef]
139. Guan, H.; Zhou, X.; Wen, W.; Jin, B.; Li, J.; Zhang, S. Efficient and Robust Cu/TiO_2 Nanorod Photocatalysts for Simultaneous Removal of Cr(VI) and Methylene Blue under Solar Light. *J. Chin. Chem. Soc.* **2018**, *65*, 706–713. [CrossRef]
140. Traid, H.D.; Vera, M.L.; Ares, A.E.; Litter, M.I. Advances on the synthesis of porous TiO_2 coatings by anodic spark oxidation. Photocatalytic reduction of Cr(VI). *Mater. Chem. Phys.* **2017**, *191*, 106–113. [CrossRef]
141. Naranjo-Castaño, N.V.; Chacón-Chamorro, M.; Rosero-Rodríguez, F.N.; Jiménez-García, F.N.; Acevedo, N.A.; García-Gallego, Y.P.; Lubo-Mestanza, C.A.; Riaño-Rojas, J.C.; Restrepo-Parra, E. Photocatalytic reduction of Cr(VI) in wastewater using TiO_2 coatings synthesized by plasma electrolytic oxidation (PEO): Influence of duty cycle and EDTA addition. *Next Mater.* **2026**, *11*, 101727. [CrossRef]
142. Zulkifli, M.A.; Bashirom, N.; Kian, T.W.; Kawamura, G.; Matsuda, A.; Lockman, Z. Rapid TiO_2 Nanotubes Formation in Aged Electrolyte and Their Application as Photocatalysts for Cr(VI) Reduction Under Visible Light. *IEEE Trans. Nanotechnol.* **2018**, *17*, 1106–1110. [CrossRef]
143. Altın, İ.; Sökmen, M. Photocatalytic Properties of Silver Incorporated Titania Nanoparticles Immobilized on Waste-Derived Polystyrene. *Water Air Soil Pollut.* **2014**, *225*, 1786. [CrossRef]
144. Zhang, L.; Xing, Z.; Zhang, H.; Li, Z.; Zhang, X.; Zhang, Y.; Li, L.; Zhou, W. Multifunctional Floating Titania-Coated Macro/Mesoporous Photocatalyst for Efficient Contaminant Removal. *ChemPlusChem* **2015**, *80*, 623–629. [CrossRef] [PubMed]
145. Yan, W.; Chen, Q.; Meng, X.; Wang, B. Multicycle photocatalytic reduction of Cr(VI) over transparent PVA/TiO_2 nanocomposite films under visible light. *Sci. China Mater.* **2017**, *60*, 449–460. [CrossRef]
146. Yu, C.; Mao, D.; Xia, F.; Huang, X.; Li, J.; Liu, W.; Fang, D. Formation of SnS_2/Ni_2S_3 heterojunction on three-dimensional nickelframework for treating chromium(VI)-containing wastewater. *Mater. Res. Express* **2017**, *4*, 115023. [CrossRef]
147. de Bittencourt, M.A.; Novack, A.M.; Scherer Filho, J.A.; Mazur, L.P.; Marinho, B.A.; da Silva, A.; de Souza, A.A.U.; de Souza, S.M.A.G.U. Application of $FeCl_3$ and TiO_2-coated algae as innovative biophotocatalysts for Cr(VI) removal from aqueous solution: A process intensification strategy. *J. Clean. Prod.* **2020**, *268*, 122164. [CrossRef]
148. Djellabi, R.; Yang, B.; Adeel Sharif, H.M.; Zhang, J.; Ali, J.; Zhao, X. Sustainable and easy recoverable magnetic TiO_2-Lignocellulosic Biomass@Fe_3O_4 for solar photocatalytic water remediation. *J. Clean. Prod.* **2019**, *233*, 841–847. [CrossRef]
149. Arif, Z.; Sethy, N.K.; Mishra, P.K.; Verma, B. Green approach for the synthesis of ultrafiltration photocatalytic membrane for tannery wastewater: Modeling and optimization. *Int. J. Environ. Sci. Technol.* **2020**, *17*, 3397–3410. [CrossRef]
150. Jyothi, M.S.; Nayak, V.; Padaki, M.; Balakrishna, R.G.; Soontarapa, K. Eco-friendly membrane process and product development for complete elimination of chromium toxicity in wastewater. *J. Hazard. Mater.* **2017**, *332*, 112–123. [CrossRef] [PubMed]
151. Machado, T.C.; Lansarin, M.A.; Matte, N. Reduction of hexavalent chromium: Photocatalysis and photochemistry and their application in wastewater remediation. *Water Sci. Technol.* **2014**, *70*, 55–61. [CrossRef] [PubMed]
152. Chang, Y.-H.; Wu, M.-C. Enhanced photocatalytic reduction of Cr(VI) by combined magnetic TiO_2-based NFs and ammonium oxalate hole scavengers. *Catalysts* **2019**, *9*, 72. [CrossRef]
153. Liu, X.; Liu, G.; You, S. Effective in-situ reduction of Cr(VI) from leather wastewater by advanced reduction process based on $CO_2^{\cdot-}$ with visible-light photocatalyst. *Chemosphere* **2021**, *263*, 127898. [CrossRef] [PubMed]
154. Castiblanco, Y.; Perilla, A.; Arbelaez, O.; Velasquez, P.; Santis, A. Effect of the pH and the Catalyst Concentration on the Removal of Hexavalent Chromium (Cr(VI)) During Photocatalysis of Wastewater from Plating on Plastics Industry. *Chem. Eng. Trans.* **2021**, *86*, 679–684. [CrossRef]

155. Liu, X.H.; Xing, Z.H.; Chen, Q.Y.; Wang, Y.H. Multi-functional photocatalytic fuel cell for simultaneous removal of organic pollutant and chromium (VI) accompanied with electricity production. *Chemosphere* **2019**, *237*, 124457. [CrossRef] [PubMed]
156. Shen, J.H.; Jiang, Z.W.; Liao, D.Q.; Horng, J.J. Enhanced synergistic photocatalytic activity of TiO_2/oxidant for azo dye degradation under simulated solar irradiation: A determination of product formation regularity by quantifying hydroxyl radical-reacted efficiency. *J. Water Process Eng*. **2021**, *40*, 101893. [CrossRef]

Disclaimer/Publisher's Note: The statements, opinions and data contained in all publications are solely those of the individual author(s) and contributor(s) and not of MDPI and/or the editor(s). MDPI and/or the editor(s) disclaim responsibility for any injury to people or property resulting from any ideas, methods, instructions or products referred to in the content.